A new multilayered visco-elasto-plastic experimental model to study strike-slip fault seismic cycle

Yannick Caniven, Stephane Dominguez, Roger Soliva, Rodolphe Cattin, Michel Peyret, M. Marchandon, Christian Romano, Vincent Strak

AGU PUBLICATIONS

Tectonics

RESEARCH ARTICLE
10.1002/2014TC003701

Key Points:
- Seismic cycle on a strike-slip fault is simulated using a new experimental model
- Realistic rheologic, tectonics and kinematics boundary conditions are used
- Main mechanisms and kinematics related to the seismic cycle are well reproduced

Supporting Information:
- Readme
- Table S1
- Table S2
- Table S3

Correspondence to:
S. Dominguez,
dominguez@gm.univ-montp2.fr

Citation:
Caniven, Y., S. Dominguez, R. Soliva, R. Cattin, M. Peyret, M. Marchandon, C. Romano, and V. Strak (2015), A new multilayered visco-elasto-plastic experimental model to study strike-slip fault seismic cycle, *Tectonics*, *34*, 232–264, doi:10.1002/2014TC003701.

Received 12 AUG 2014
Accepted 25 DEC 2014
Accepted article online 7 JAN 2015
Published online 12 FEB 2015

A new multilayered visco-elasto-plastic experimental model to study strike-slip fault seismic cycle

Y. Caniven[1], S. Dominguez[1], R. Soliva[1], R. Cattin[1], M. Peyret[1], M. Marchandon[2], C. Romano[1], and V. Strak[3]

[1]Géosciences Montpellier Laboratory, University of Montpellier, Montpellier, France, [2]Géoazur Laboratory, University of Nice Sophia–Antipolis, Valbonne, France, [3]School of Geosciences, Monash University, Clayton, Victoria, Australia

Abstract Nowadays, technological advances in satellite imagery measurements as well as the development of dense geodetic and seismologic networks allow for a detailed analysis of surface deformation associated with active fault seismic cycle. However, the study of earthquake dynamics faces several limiting factors related to the difficulty to access the deep source of earthquake and to integrate the characteristic time scales of deformation processes that extend from seconds to thousands of years. To overcome part of these limitations and better constrain the role and couplings between kinematic and mechanical parameters, we have developed a new experimental approach allowing for the simulation of strike-slip fault earthquakes and analyze in detail hundreds of successive seismic cycle. Model rheology is made of multilayered visco-elasto-plastic analog materials to account for the mechanical behavior of the upper and lower crust and to allow simulating brittle/ductile coupling, postseismic deformation phase and far-field stress transfers. The kinematic evolution of the model surface is monitored using an optical system, based on subpixel spectral correlation of high-resolution digital images. First, results show that the model succeed in reproducing the deformation mechanisms and surface kinematics associated to the main phases of the seismic cycle indicating that model scaling is satisfactory. These results are comforted by using numerical algorithms to study the strain and stress distribution at the surface and at depth, along the fault plane. Our analog modeling approach appears, then, as an efficient complementary approach to investigate earthquake dynamics.

1. Introduction

Destructive earthquakes, like the recent Haiti earthquake (2010, $M_w = 7$, >230,000 deaths), generate heavy economic and human losses. Therefore, understanding the dynamics of geological processes that trigger these natural disasters represents a major scientific and societal issue. Earthquake study faces, however, several limiting factors related to the difficulty of accessing the deep source of earthquakes and integrating the characteristic time scales of deformation processes that extend from seconds to thousands of years [*Ben-Zion*, 2008]. Moreover, our knowledge of earthquake mechanics is very recent (<100 years). It is only after the 1906 great San Francisco earthquake that the elastic rebound theory [*Reid*, 1910] proposed a theoretical framework to explain observed surface deformation associated with the different phases of the seismic cycle.

New technological advances in remote sensing measurements as well as the development of dense and permanent geodetic and seismological networks now allow for a detailed analysis of both surface deformation and fault kinematics. These data are essentially interpreted using analytical and numerical modeling approaches to assess deformation processes, physical properties of faults, the effect of strain and stress boundary conditions [e.g., *King et al*., 1994; *Wald et al*., 1996; *Delouis et al*., 2002; *Avouac et al*., 2014]. Most of these studies consider the seismogenic crust as an homogeneous elastic half-space to model coseismic and interseismic deformation via rectangular dislocation and point source models [*Okada*, 1985, 1992], finite elements models, [e.g., *Vergne et al*., 2001; *Chéry et al*., 2001a, 2001c], or block models [e.g., *Meade and Hager*, 2005]. Some of these approaches integrate additional parameter and processes; the visco-elastic response of the lower crust to study postseismic deformations processes [e.g., *Nur and Mavko*, 1974; *Perfettini and Avouac*, 2004; *Wang et al*., 2012] or lateral variations of elastic thickness to study the role of the brittle/ductile transition depth on the interseismic surface strain field [e.g., *Chéry*, 2008; *Jolivet et al*., 2008].

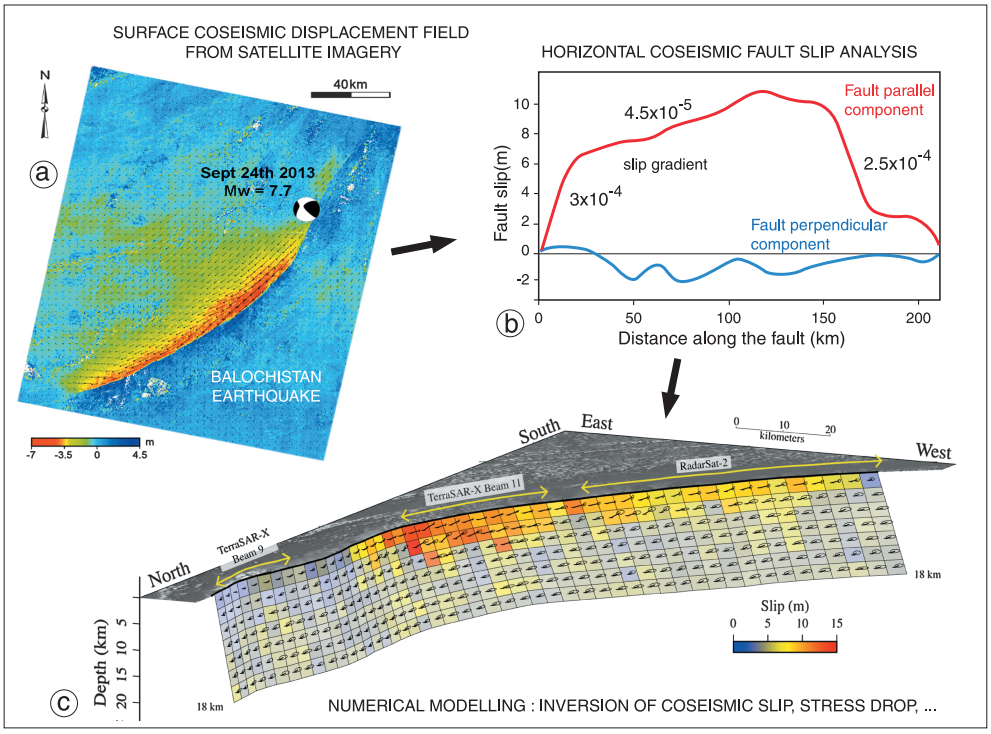

Figure 1. Example of a recent earthquake case study; the 2013 Balochistan earthquake (modified from *Avouac et al.* [2014] and *Jolivet et al.* [2014]). (a) Accurate surface deformation measurements, derived from subpixel satellite image correlation and InSAR interferometry, allow for (b) a detail analysis of earthquake surface horizontal coseismic slip. (c) Numerical modeling is used to obtain complementary information about deformation processes mechanics, physical properties of faults, and boundary conditions. Here slip along the fault plane is inverted from geodetic surface displacement field.

Recent numerical developments allow to simulate all the phases of the main seismic cycle, including fast and slow slip episodes [*Lapusta et al.*, 2000; *Van Dinther et al.*, 2013].

However, despite these significant improvements, the effect of important parameters, such as friction heterogeneities on the fault plane or stress transfers induced by past earthquakes are not yet well understood to be efficiently modeled.

The recent $M_w = 7.7$ Balochistan earthquake of 24 September 2013 is a striking example of the progress and remaining difficulties that characterize our knowledge of earthquake mechanics [*Avouac et al.*, 2014; *Jolivet et al.*, 2014]. Coseismic ground surface deformation was first measured accurately from subpixel correlation of Landsat-8 satellite images and interferometric synthetic aperture radar (InSAR) processing of radar satellite images then combined with back-projection and finite source modeling of teleseismic waveforms (Figure 1). Based on these data, key properties and characteristics of this earthquake were determined: fault kinematics and surface displacement field, earthquake nucleation and slip propagation dynamics on the fault plane, rupture speed, and directivity. However, because fault parameters (geometry, frictional properties, and others) and interseismic loading history are poorly documented, the geological processes that control earthquake nucleation and the mechanics of rupture propagation remain difficult to study. Furthermore, the observation time scale is yet too short to constrain the fault behavior variability, i.e., creeping or locking, during the whole interseismic phase.

The occurrence of a major earthquake on the North Anatolian Fault (NAF) likely affecting the city of Istanbul clearly illustrates the consequences of these limitations and the need to find new complementary approaches. If most of scientists agree to consider that the next earthquake will rupture the Marmara Sea fault segment, it is still impossible to determine precisely its timing and future magnitude [e.g., *Le Pichon et al.*, 2001; *Armijo et al.*, 2005]. This has, of course, significant consequences to define the mitigation levels required to limit economic and human losses induced by the forthcoming earthquake.

To improve our capability to predict the location and the size of future earthquakes, numerous scientific questions that are still debated must find an answer:

1. How does interseismic strain field evolve through time between two successive major earthquakes? Is there any velocity variation or anomaly that could be studied to better constrain the characteristics of the next coseismic rupture?
2. What is the effect of fault friction heterogeneities along the fault plane; both on seismic coupling (stick-slip versus creep) and on earthquake dynamics?
3. How do crustal rheology and tectonic boundary conditions (effective elastic thickness, brittle/ductile transition depth, fault kinematics, loading rate, and others) modify the kinematics and mechanics of coseismic and interseismic surface deformations?
4. How does the coseismic rupture propagates along the fault plane? What are the parameters that control its initiation, direction of propagation, and stop?

To afford new data to answer these questions, we have developed a complementary approach based on analog modeling of crustal deformation associated to strike-slip faulting at the seismic cycle timescale. With this aims, we designed a new type of experimental setup, coupled to numerical modeling analysis tools, that enable the simulation of microearthquakes and the deformation phases associated with the seismic cycle (coseismic, postseismic, and interseismic). Our main objectives are to study experimentally the mechanisms and couplings that control both surface and deep crustal deformation in order to improve the interpretation of geological observations and geophysical and seismological measurements.

Because this paper is our first project publication, it is mainly devoted to describe the experimental protocol and the validation of the analog modeling scaling through a comparison between preliminary experimental results and available geophysical data. Model potentialities and limitations as well as possible new fields of investigation will also be discussed. Scientific results will be only evoked and will be presented in forthcoming publications using this methodological paper as a base.

2. State of the Art in Experimental Modeling of Earthquakes

Analog modeling is widely used to study geological processes, including earthquakes and seismic cycle [e.g., *Ohnaka*, 1973; *Ohnaka et al*., 1987; *Hamilton and McCloskey*, 1997; *Nasuno et al*., 1998; *Xia* et al., 2004; *Lykotrafitis et al*., 2006]. In parallel to analytical and numerical approaches, several experimental models have been developed in the last decades to investigate seismic deformation mechanisms [*Brune*, 1973; *Ohnaka*, 1973; *Hamilton and Mccloskey*, 1997; *Brune and Anooshehpoor*, 1998; *Nasuno et al*., 1998]. These models, called physics or analogs, can be divided into three main categories according to their degree of similarity with nature. The first ones correspond to unscaled mechanical models [*Hubbert*, 1937] such as the spring box models [*Brace and Byerlee*, 1966; *Byerlee*, 1970; *Brace*, 1972] which allow to reproducing successfully fault stick-slip dynamics. They are constituted by rigid blocks in motion through elastic springs or viscoelastic coupling devices sliding on a frictional interface. This type of models is mainly used to illustrate the couplings controlling the mechanical behavior of the crust or the lithosphere. Despite their apparent simplicity, they helped to better constrain the relationships between fault frictional slip and the characteristics of seismicity on the fault or at the crustal scale (e.g., multiblocks and springs model of *Burridge and Knopoff* [1967]). Spring block models are still developed today, mainly using numerical modeling approaches [e.g., *Carlson and Langer*, 1989; *Wang*, 2012].

The second category is focused on earthquake rupture dynamics at the scale of an analog fault plane. These experimental models are generally composed of two elastic blocks, sliding on top of each other by frictional contact (Figure 2a). They are more sophisticated than spring block models because they integrate a physical and mechanical first-order scaling (conserving normal and shear stress ratio between model and nature, physical parameters scaling; stiffness modulus, Poisson coefficient, and others). One of the first and most interesting example is the original experimental device developed by *Brune* [1973] to study rupture dynamics along precut surfaces in foam rubber. This model obtained good results in studying the effects of static and dynamic friction on the coseismic slip kinematics and mechanics. Since then, the fields of application of foam rubber models were extended to include the study of frictional heat generation in the fault zone and also seismic waves radiation [*Brune*, 1996; *Anooshehpoor and Brune*, 1994, 1999]. Using a similar approach, other researchers investigated fault rupture dynamics by studying fault slip into natural

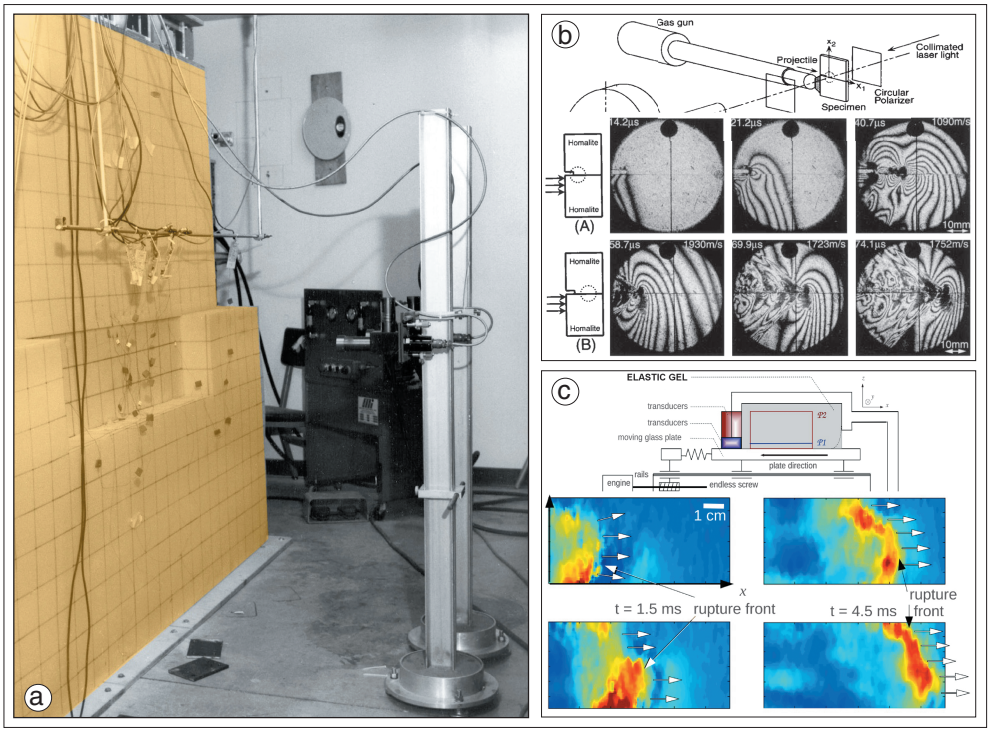

Figure 2. (a) Experimental setup made of two large foam rubber blocks used to study frictional sliding and associated seismic wave propagation [e.g., *Brune and Anooshehpoor*, 1998]. (b) Photoelasticity setup (polariscope + 2 Mfps high-speed camera) use to study supershear crack propagation in Homalite-100 plastic media [e.g., *Rosakis et al*., 1999]. (c) PVA Elastic gel friction experiment equipped with tranducer allowing to image rupture propagation [e.g., *Latour et al*., 2013].

rocks [e.g., *Passelegue et al*., 2013] or shear crack propagation into plastic analog materials [e.g., *Rosakis et al*., 1999; *Mello et al*., 2010; *Nielsen et al*., 2010; *Schubnel et al*., 2011]. For these last experiments, model monitoring is achieved using photoelasticity in conjunction with very high speed photography which allow analyzing in detail rupture initiation and propagation processes (Figure 2b). Obtained results have become famous for being the first to propose an explanation to the supershear coseismic rupture velocities, observed on several major earthquakes [e.g., *Bouchon et al*., 2010]. Recently, *Latour et al*. [2011a, 2011b, 2013] developed another original experimental setup to study rupture dynamics in a PVA (PolyVynilAlcool) gel block sliding on a frictional interface. Failure dynamics is monitored using ultrafast ultrasonic speckle interferometry which allows for a near real time observation of rupture front propagation (Figure 2c). However, if these types of analog model can be used to evidence strain processes at the fault plane, their rheology is generally too simplified to compare the experimental results with geodetic and geophysical far-field data.

Recently, a third set of analog model and experimental setup has been developed, specifically to study subduction earthquakes. These models are the first 2-D scaled analog models reproducing the main strain mechanisms characterizing the seismic cycle, i.e., from the short to the long spatial and temporal scale, [e.g., *Rosenau et al*., 2009; *Corbi et al*., 2013]. Model deformations are monitored using Particle Image Velocimetry (PIV) techniques. *Rosenau et al*. [2009] use a prism composed by a mixture of elastoplastic granular particles above a viscoelastic mantle wedge made of silicone oil. The seismogenic zone is simulated using a layer of rice grains whose frictional behavior is velocity weakening. *Corbi et al*. [2013] use a viscoelastic gelatin [*Di Giuseppe et al*., 2009] prism, simulating the continental lithosphere and slipping at a low-angle tilted plane. The seismogenic zone is simulated by a velocity-weakening gel-sandpaper interface bounded toward the surface and at depth by two velocity-strengthening frictional interfaces [*Corbi et al*., 2011, 2013]. Advantages of these models are their capability to generate several consecutive seismic cycles and the use of realistic boundary conditions allowing, to some extent, for the extrapolation of experimental results to the nature. The limits of these models are mainly linked to their 2-D design and to the rheology used which consists of a homogeneous elastoplastic material (gelatin or granular particles).

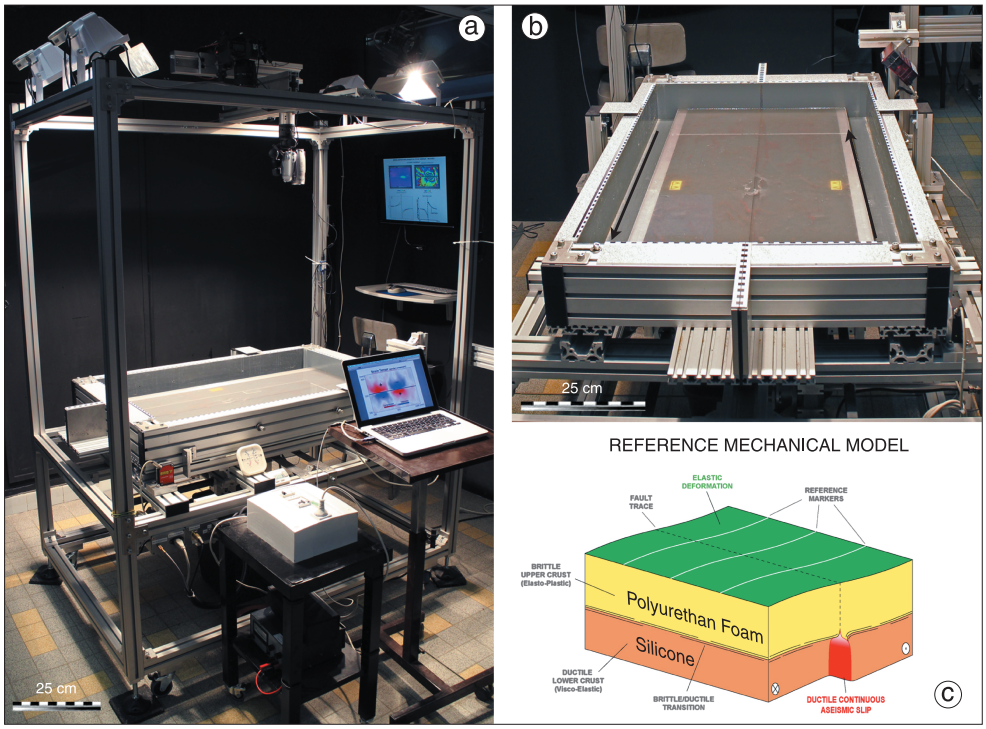

Figure 3. (a) General view of the experimental setup. The device is constituted by a computerized shear box fixed to a rigid aluminum structure. A digital subpixel image correlation system is used to monitor model surface deformation. (b) Zoom on the shear box. Here only the basal silicone layer is shown at bottom of the box. Black arrows indicate the displacement direction of the rigid compartments. (c) Reference mechanical model. Mechanical and kinematical boundary conditions are based on the elastic rebound model [*Reid*, 1910]. Model visco-elasto-plastic rheology is achieved by using two elastic polyurethane foam plates in frictional contact on their lengths, superimposed on a ductile basal silicone layer.

In line with these later works, we have developed a new experimental device whose mechanical model is based on the elastic rebound theory [*Reid*, 1910], to simulate the seismogenic behavior of a strike-slip fault (Figure 3). It differs from previous analog model on several points. First, we use a multilayered rheology to simulate the mechanical behavior of the elastic upper crust and the viscoelastic lower crust at the seismic cycle time scale. Second, we integrate realistic tectonics and kinematics boundary conditions characterizing strike-slip fault geologic setting. Third, we constrained and modified the physical and mechanical properties of the fault plane to improve model scaling. As demonstrated hereafter, these characteristics allow for a nearly direct comparison between model kinematics and geodetic measurements on active strike-slip faults.

3. Analog Modeling Protocol

3.1. Experimental Set Up and Boundary Conditions

The experimental device consists of a 1 m × 1.5 m × 1.8 m rigid structure of extruded aluminum profiles supporting all mechanical and model monitoring equipments (Figure 3a). Considering that model deformation ranges within a few tens of microns, special attention has been paid to ensure that the device does not deform during the experiment. To reduce potential external sources of vibrations, the four feet of the device are equipped with shock absorbers. The main structure supports two compartments mounted on two horizontal linear-guided systems controlled by a computerized motoreductor (Figure 3b). Both compartments have similar sizes of 1.21 m × 0.73 m × 0.12 m and are in contact along their longest dimension. They represent the two compartments of a strike-slip fault and move in opposite direction at a constant velocity that can vary from 1 to 7 μm/s (0.35 cm/h to 2.5 cm/h). Compartment displacements are measured using a laser telemeter and image processing analysis (see section 3.4). Analog materials that are placed into the two compartments are submitted to a localized shear deformation at an imposed constant velocity (or loading rate).

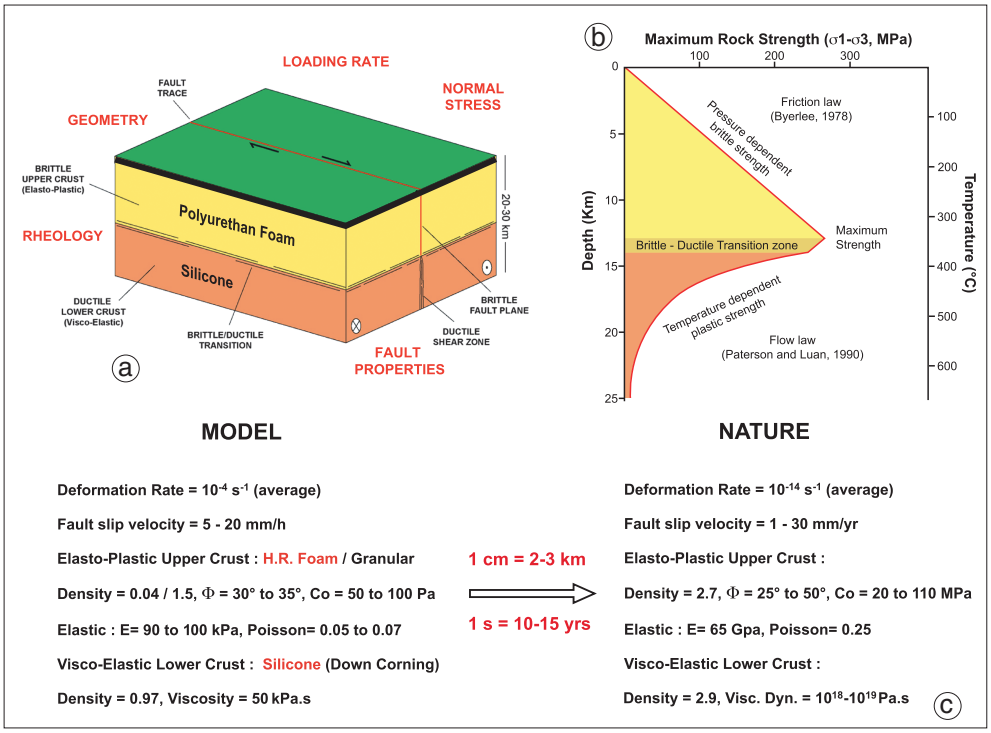

Figure 4. The model is constituted by (a) three main superimposed layers of different analog materials whose physical properties were scaled down to simulate (b) the mechanical behavior of an idealized continental crust. The basal layer is made of a viscoelastic silicone compound. The upper layer is made of a high-resilience Polyurethane elastic foam. (c) Model to nature mechanical and physical properties comparisons and expected first-order spatial and temporal model scaling.

The analog model material can be prestressed laterally to scale the initial normal stress along the fault plane (from 50 to 1000 Pa) and also adjust the threshold of static and dynamic friction (see section 3.2). At a local scale, normal stress variations along the fault depends on the contact geometry between the two polyurethane foam plates induced by industrial surface cutting irregularities. Strain associated to the prestressing stage is quantified by subpixel correlation of two photos taken before and after putting the foam plates in contact. Normal stress along the surface fault trace is estimated using the measured strain field, the foam Young modulus and the Hooke's law.

3.2. Model Rheology and First-Order Scaling

Model rheology was determined to fit the requirements of the elastic rebound theory developed by Reid in 1910 to explain the surface deformations associated to the great 1906 San Francisco earthquake [e.g., *Savage and Prescott*, 1978; *Thatcher and Rundle*, 1984; *Matsuura and Sato*, 1989; *Savage*, 1983, 1990]. This simple mechanical model considers that active faults slip continuously along ductile shear zones in the viscoelastic lower crust but episodically along frictional fault planes in the elastoplastic upper crust [e.g., *Tse and Rice*, 1986; *Li and Rice*, 1987; *Bufe and Varnes*, 1993]. This model is behind the definition of the deformation phases (interseismic, coseismic, and postseismic) and the notion of seismic cycle [e.g., *Weldon et al.*, 2004], which implies both repeatability and predictability of these phases at the time scale of, at least, several hundred years.

Our analog model is formed by three superimposed layers of different analog materials whose physical properties were selected to simulate the mechanical behavior of an idealized continental crust (Figures 4a and 4b). Main nature and model parameters are summarized in Figure 4c. Due to technical constraints related to the maximum size of the experimental setup and the need to model a sufficiently large portion of the crust, we expected spatial and temporal dimensioning to be 1 cm in the model is equal to 2–3 km and 1 s in the model is equal to 10–15 years, respectively.

The basal layer is 3 cm thick and is made of a viscoelastic silicone compound (Polydimethyl-siloxane polymer PDMS-SGM 36, Dow Corning Ltd., viscosity about 50 kPa s at room temperature). This type of analog material has been extensively used to study experimentally crustal or lithospheric deformation [*Davy and Cobbold*, 1991; *Baby et al*., 1995; *Faccenna et al*., 1999; *Bonini et al*., 2000; *Koyi and Skelton*, 2001]. The silicone layer allows for simulating the viscous deformation and strain-hardening behavior of the lower crust (depth $>$ 10–15 km). Indeed, at this depth, the temperature reaches more than 350°C and the resistance of the crust is mainly controlled by viscoplastic forces (Figure 4b). Therefore, the main mechanical parameter to consider is the viscosity of the crust, which is strain and temperature dependent and ranges from 10^{18} to 10^{19} Pa s at the scale of the seismic cycle in active tectonic contexts [e.g., *Bürgmann and Dresen*, 2008; *Bruhat et al*., 2011; *Wen et al*., 2012].

The intermediate layer is 4 to 6 cm thick and it is made of a high-resilience Polyurethane foam (Young modulus = 95 ± 10 kPa, Poisson ratio = 0.06 ± 0.02, shear modulus = 45 ± 5 kPa, Vp = 100 m/s, Vs = 68 m/s). The foam has a high elasticity, which largely dominates its mechanical behavior. Its viscosity is unknown but considered as high enough to be neglected in the process of model scaling. The foam allows for the simulation of the elastic deformation that characterizes the upper crust (depth $<$ 10–15 km) mechanical behavior at the time scale of the seismic cycle. The brittle/ductile transition corresponds to a, 2–3 mm thick, impregnation of the silicone into the base of the polyurethane foam, insuring a strong coupling whose mechanical properties depend also on model velocity boundary conditions (elastic loading rate).

The uppermost layer is 0.25 to 0.5 cm thick and is formed by a granular material mixture (silica powder and graphite). It represents the very upper kilometers of the shallow crust where deformation is considered as essentially brittle [e.g., *Byerlee*, 1968, 1978]. This very thin layer is mainly used to cover the model with a color rich texture in order to improve the monitoring of surface deformation.

Extrapolation of analog modeling results to nature is based on the scaling theory elaborate by *Hubbert* [1937] and later refined by *Horsfield* [1977], *Ramberg* [1981], *Davy and Cobbold* [1991], and *Cobbold and Jackson* [1992]. This theory postulate that an experimental model can be considered as properly scaled to nature if geometric, kinematics, and dynamics similitude rules are respected. As mentioned before, we expected the geometric factor (L^*) to be in the range between 3×10^{-6} and 5×10^{-6} (1 cm in the model corresponds to 2–3 km in nature). The geometric rule implies also that model parameters issue from length ratios such as angles (fault dip), deformation (ε), or Poisson coefficient (ν) should be identical to nature. More generally, the scaling theory postulates that all dimensionless parameters like gradients (strain, stress) and friction (μ) should be as close as possible to those of the nature. From a mechanical point of view, the scaling theory indicates that mechanical stress (σ) and forces must be reduced using the geometric factor, modulated by the model to nature density ratio in a normal gravity field ($L^* = \sigma^* \cdot \rho^* \cdot g^*$). The upper crust is modeled using a polyurethane foam plate which has a low density ($\rho = 40$ kg m^{-3}) compare to upper crust density (2700 kg m^{-3}). As a result, the lithostatic stress and the normal stress along the fault plane are very low inducing possible model scaling distortion. We decide to compensate this limitation by imposing the initial normal stress along the fault plane (~500 Pa) such as it scales to nature (~150 MPa) using the geometric factor ($L^* \sim 4 \times 10^{-6}$). Similarly, we select a specific polyurethane foam whose shear modulus ($G = 45 \pm 5$ kPa) scales to nature ($G \sim$ 10–30 GPa) using the same factor (L^*).

Temporal scaling evaluation is difficult to constrain for several reasons. First, the different phase of the seismic cycle are characterized by extremely variable deformation rates ranging for the interseismic phase from 10^{-5} s^{-1} (elastic loading) to 10^{-4} s^{-1} (fault creep) and for the coseismic phase from 10^{-2} s^{-1} (coseismic fault slip) to $>$ 10 s^{-1} (coseismic rupture). Hereafter, we follow the methodology, adopted by *Rosenau et al*. [2009] and *Corbi et al*. [2013] and defined two different timescales for the interseismic and the coseismic phases. During the interseismic slow deformation, inertia forces are negligible but viscous forces in the silicone layer, representing the lower crust, become dominant. Consequently, the interseismic timescale (Ti*), can be determined using the following relation [e.g., *Weijermars and Schmeling*, 1986]:

$$T_i^* = \frac{\eta^*}{\sigma^*} \tag{1}$$

where η^* is the model/nature ratio of viscosity. For a silicone viscosity of 5×10^4 Pa s and considering a mean lower crust viscosity of 5×10^{18} Pa s in active tectonic contexts [e.g., *Bürgmann and Dresen*, 2008; *Bruhat et al*., 2011; *Wen et al*., 2012], the model/nature ratio of viscosity is ~ 10^{-14}. Using $\sigma^* = L^* = 4 \times 10^{-6}$, we obtain, then, an interseismic timescale of $T_i^* \sim 2.5 \times 10^{-9}$ (i.e., 1 s in the model is equal to about 10–15 years in nature).

Table 1. Model Scaling Parameters[a]

Parameters	Symbol	Dimension (MLT)	Unit	Model (M)	Nature (N)	Scaling Factor (M/N)
		Physic				
Upper crust density (mean)	ρuc	M/L^3	kg/m^3	45	2700	1.7×10^{-2}
Lower crust density (mean)	ρlc	M/L^3	kg/m^3	970	2900	3×10^{-1}
		Geometric				
Length (Fault length)	Lf	L	m	1	2.5×10^{5}	4×10^{-6}
Coseismic fault slip (mean)	D_{mean}	L	m	1×10^{-4}	25	4×10^{-6}
Surface aspect ratio	Sar	L	m	~5	~5	~1
		Mechanic				
Upper crust shear modulus	Gc	M/LT^2	Pa	5×10^{4}	$\sim10^{10}$	5×10^{-6}
Upper crust Poisson ratio	ν	-	-	0.06	0.25	0.24
Upper crust friction coefficient	μ	-	-	0.65	0.4	1.6
Friction rate	$a-b$	-	-	~ -0.02	-0.015	~1
Upper crust stress	σ	M/LT^2	Pa	500	1.5×10^{8}	3×10^{-6}
Coseismic slip gradient (mean)	γco	-	-	5×10^{-4}	5×10^{-5}	10
Lower crust viscosity	ηlc	M/LT	Pa s	5×10^{4}	5×10^{18}	10^{-14}
		Kinematic				
Gravitational acceleration	g	L/T^2	$m\,s^{-2}$	9.8	9.8	1
Strain rate (mean)	$\dot{\varepsilon}$	T^{-1}	s^{-1}	10^{-4}	10^{-14}	1×10^{10}
Mean velocity (interseismic)	Vi	L/T	$m\,s^{-1}$	3×10^{-6}	2×10^{-9}	1500
Mean velocity (coseismic)	Vc	L/T	$m\,s^{-1}$	3×10^{-3}	1.5	2×10^{-3}
Rupture velocity (mean)	Vr	L/T	$m\,s^{-1}$	>10	3×10^{3}	3×10^{-3}
Coseismic D_{max}/Daverage	γD	-	-	~1.7	~1.8	1
Time (interseismic duration)	Ti	T	s	100	4×10^{10}	2.5×10^{-9}
Time (coseismic duration)	Tc	T	s	0.05	25	2×10^{-3}
		Energetic				
Seismic moment	Mo	ML^2/T^2	N m	1.6×10^{-1}	3×10^{20}	5.3×10^{-22}
Coseismic stress drop	$\Delta\tau$	M/LT^2	Pa	~40	3×10^{6}	1.4×10^{-5}

[a]Model and nature parameters are used to calculate scaling factors and evaluate model analogy in terms of geometry, kinematics, and dynamics.

As noticed by *Corbi et al*. [2011], the coseismic timescale (T_c^*) can be estimated considering that the Froude number should remain constant ($Fr^* = 1 = (L^*/T_c^*)/\sqrt{(g^* \cdot L^*)}$. As a result, $T_c^* = \sqrt{L^*} = 2\times10^{-3}$ (so 1 s in the model is equal to approximately 500 s in nature). As describe more in detail in section 4.1, microquake coseismic phase duration is 50 ms in average which scale to about 25 s in nature, consistent with seismological data [e.g., *Bouchon et al*., 2002]. As proposed by *Rosenau et al*. [2009], we estimate the interseismic and coseismic stage velocities using the ratios between L^* and T_i^* ($Vi^* \sim 1600$) and L^* and T_c^* ($Vc^* \sim 2\times10^{-3}$). We obtain for the interseismic phase; 5 mm/h in the model is equal to 27 mm/yr in nature and for the coseismic phase; $3\times10^{-3}\,m\,s^{-1}$ in the model is equal to 1.5 m/s.

This first-order model scaling will be discussed more in detail during the description of model kinematical and mechanical behaviors, as well as in the discussion (section 5) where all the scaling parameters are summarized in a table (Table 1).

3.3. Physical and Mechanical Properties of the Fault Plane

The fault plane is materialized by the contact zone between the two foam plates. It measures 1 m long and extends vertically 8–10 cm from the base of the two rigid aluminum profile compartments up to the model surface through the silicone, polyurethane foam, and granular material layers. Friction properties evolves, then, vertically along the fault plane depending on the material that is crossed. Near the model surface, the fault plane crosscuts the thin granular material layer whose mechanical properties are characterized by a cohesion of 50 to 100 Pa and an internal friction of 0.6 ± 0.05. Because this layer is far thinner than the two others (generally less than 5 mm), its role on fault slip behavior is neglected. The main frictional interface is constituted by the intermediate layer along which the two foam plates slip in opposite direction. At fault tips, two low-friction patches, 3 cm long, were sticked on each side of the fault plane to limit free boundary effects. These patches induce a stable sliding of the polyurethane plates in this region, allowing to restrain most of the stick-slip events in the analyzed central part of the model.

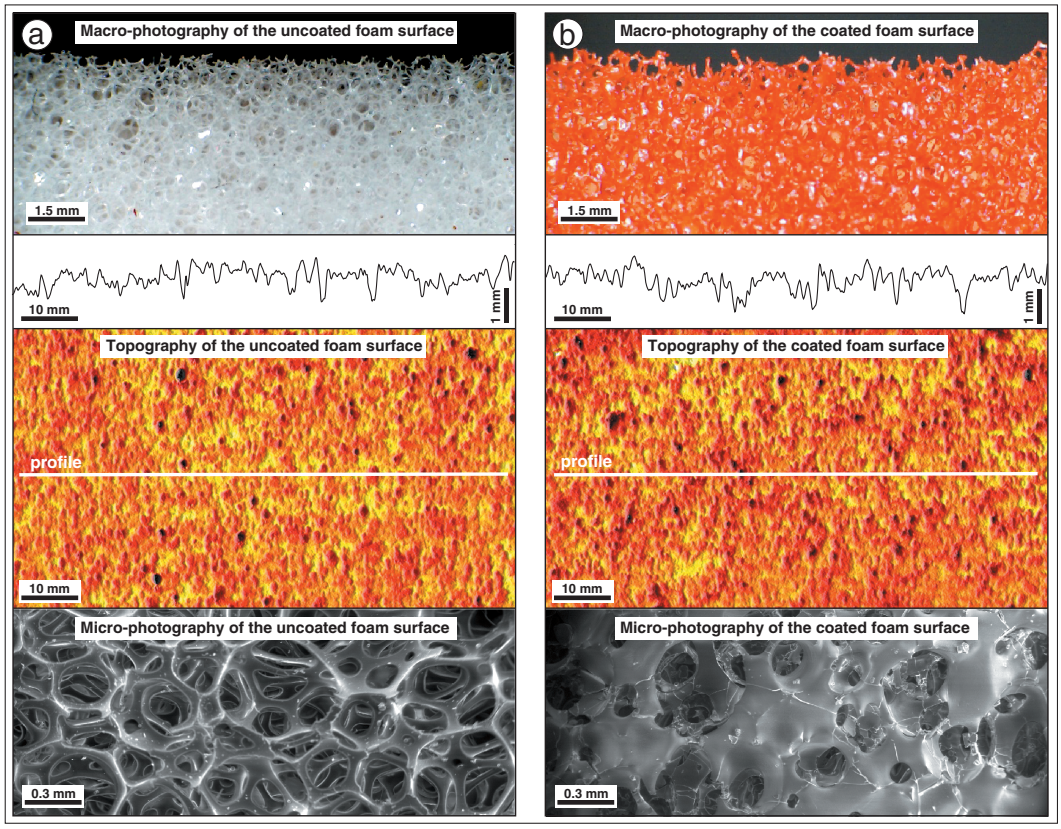

Figure 5. (a) Uncoated surface. (b) Resin coated foam surface. Analysis of foam microtopography is performed using a laser interferometer. Maximum amplitude between crest and valley is lower than 1.5 mm. The comparison between resin coated and uncoated foam surfaces indicates that the topography is only slightly modified. Foam coating induces a reduction of the friction coefficient from 2–3 (uncoated foam) to about 1 related to changes in foam surface properties at a microscopic scale.

In the basal silicone layer, the fault zone is not localized along a thin discontinuity like in the foam layer. It broadens into a ductile shear zone which resistance is shear rate dependent. Rheology of silicone SGM-36 is considered as Newtonian for strain rate below $3 \times 10^{-3}\,s^{-1}$ at 24°C and its viscosity is about 50 kPa s at this temperature [*Weijermars*, 1990; *Ten Grotenhuis et al.*, 2002]. The width of the shear zone, in the 3 cm thick ductile silicone layer, appears to be only slightly shear/strain rate dependent. Considering the range of the strain rate used in our experiments, from $3.10^{-5}\,s^{-1}$ to $10^{-4}\,s^{-1}$ (from 0.5 to 2 cm/h), the width of the shear zone is relatively constant and does not exceed 5 cm. These shear tests have been performed using the silicone layer alone (without the overlaying foam plates) to allow measuring its deformation. Consequently, the width of the ductile shear zone is most probably thinner than 5 cm.

In the Foam layer, both static and dynamic friction coefficients of the fault plane were determined experimentally using a specific direct linear shear box device (see frictional measures in the supporting information Figure S1). This device allows for shear stress measurements under different normal stress conditions. Results indicates that the foam/foam friction coefficient is very high, ranging between 2 and 3, which is unrealistic since fault friction in nature is lower than 1 [e.g., *Byerlee*, 1978]. This discrepancy was a source of criticism to *Anooshehpoor and Brune* [1994]. To decrease the friction coefficient to a more realistic value, we have performed numerous tests with the aims to modify the frictional properties of the foam surfaces. We paste, in particular, different granular powders mixtures. Finally, we spray a colored epoxy resin (RAL3000) on the two foams interface which successfully decrease the static friction coefficient to about 0.65 ± 0.2. As shown in Figure 5, the coating does not modify significantly the foam surface topography at wavelength greater than 1 mm. Figure 5 presents the results of a topographic analysis of the fault plane at the macroscopic and microscopic scales. The roughness of the fault plane appears heterogeneous on both surface types (coated and uncoated) with numerous short oscillations (wavelength 1–3 mm; amplitude

0.1–1 mm). This characteristic explains, in part, the broad variability of slip events generated during our experiments. Due to the resolution limit of the macroscopic topographic measurements, foam surface modifications can only be evidenced at a microscopic scale as revealed by EMT microscopy. The raw foam skeleton is covered by a thin (<10 μm) epoxy resin layer which connect the foam cells each others and smoothes the surface without significant stiffening of the fault zone (see indentation measurements in supporting information Figure S2).

The coated foam surface allows to conserve a stick-slip behavior as shown in the following sections. The stability of slip is usually characterized by rate and state friction laws [*Dieterich*, 1972; *Ruina*, 1983; *Scholz*, 1998] that depends on a friction rate parameter (a − b) which describes the velocity dependence of friction. It is usually determined experimentally by measuring the frictional response to step changes of slip rate. For (a − b) > 0, slip is stable, associated to a "velocity-strengthening" behavior. For (a − b) < 0, slip is unstable with occurrence of stress-drops (stick-slip), the behavior being then "velocity weakening." For our experiments, we estimate (a − b) using the following relation:

$$(a-b) = -\frac{\Delta\tau}{\sigma n.\ln\left(\frac{V_1}{V_0}\right)} \quad (2)$$

with $\Delta\tau$ the stress drop associated to stick-slip events, σn the normal stress applied to the fault, and a velocity step increase of slip from V_0 to V_1. As evoked later (section 4.1), stable slip is observed during experiments with fault slip velocities close or slightly lower than the interseismic imposed loading velocity (typically $V_0 = 5 \times 10^{-6}$ m s^{-1}). In our experiments, coseismic mean slip velocity (V_1) are in the order of a few millimeters per second, mean normal stress is 500 Pa and typical stress drop is 50 Pa (see Figure 18). Following equation (2), $(a-b)$ is about −0.017 which is very close to the 10^{-2} value determined for rocks in velocity-weakening domains, depending on temperature, normal stress, and shear rates [*Stesky et al*., 1974; *Marone et al*., 1990; *Blanpied et al*., 1991; *Marone*, 1998; *Scholz*, 1998].

3.4. Kinematics Monitoring, Data Processing, and Analysis

Assessment of surface model deformation is achieved by using several measuring equipments and image processing techniques. The main device is constituted by a CANON 5-D Mark II full frame Complementary metal-oxide semiconductor digital camera (5616 × 3744 pixels) equipped with a fixed 35 mm focal lens (distortion negligible at edges of picture), located at the top of the experimental device. It records, every 6 s (0.17 Hz), a high-resolution image of the whole model surface (Figure 6a). A video camcorder and a laser gauge are also systematically deployed for each experiment.

These imagery data are processed to analyze surface deformation kinematics using a subpixel spectral correlation algorithm (EXPCORR) developed by *Van Puymbroeck et al*. [2000] and now commonly used to measure coseismic earthquake surface deformation [e.g., *Michel and Avouac*, 2002; *Dominguez et al*., 2003; *Avouac et al*., 2006]. As for the COSI-Corr method [*Leprince et al*., 2007] EXPCORR compares the local spectral signature (interrogative square window of typically 64 × 64 pixels) of two successive images acquired by the camera and estimates the phase shift of their Fourier transform. It yields the two components of the surface displacement (*X* and *Y*) and an estimate of the signal-to-noise ratio. Measurements accuracy and spatial resolution depend on the local level of correlation of the images and the size of the sliding window. Typically, measurement accuracy is about 2 μm (RMS) and typical spatial resolution reaches one independent measurement every 5 mm. This leads to a total of about 20,000 measurement points of model surface deformation every 6 s.

Due to camera shooting geometry, only the horizontal components (*X* and *Y*) of surface displacements are measured. This feature should be taken into account when interpreting the results. This is not a strong limitation because the model experiences almost pure strike-slip faulting. Thus, the amplitude of vertical displacements are at least one order of magnitude lower than horizontal displacements. Displacements are corrected using several reference frames attached on the mobile and fixed parts of the experimental device to remove any external source of vibrations.

Once processed using the subpixel correlation algorithm, horizontal displacement data are filtered and formatted to analyze their characteristics (EW and NS components, Amplitude, vector field, displacement profile). InSAR-like interferograms are also simulated to better outline displacement gradients and coseismic rupture limits (Figure 6b). The cyclic fringes color scale outline efficiently both low and high surface

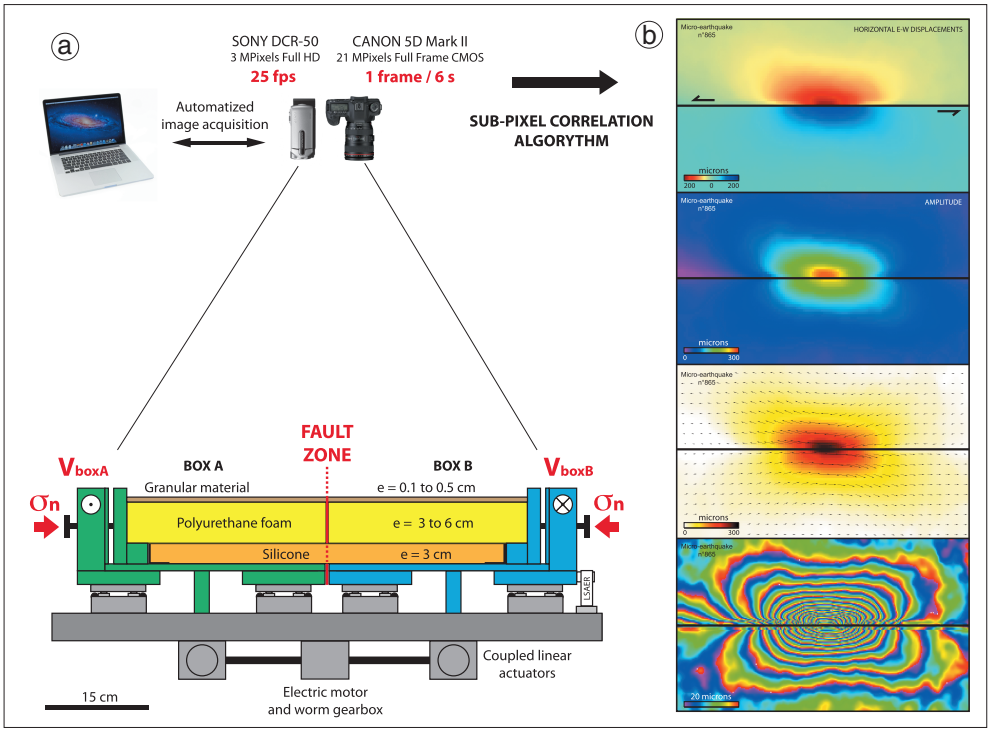

Figure 6. (a) Schematic cross section of the experimental device showing its internal mechanical structure, the geometry of analog material layers and how boundary conditions (initial normal stress and loading rate) are controlled. (b) Model surface horizontal displacements are monitored using subpixel image correlation technique. Numerical modeling tools are used to analyze model deformation at the surface and at depth.

deformation gradients. The representation also allows a direct and useful comparison with earthquake interferograms derived from InSAR satellite measurements (ERS, ALOS, and others).

4. First Experimental Results

We performed a first set of 51 experiments which are used in the present paper to describe the experimental protocol, discuss model scaling, and evaluate model potentialities. As previously mentioned, scientific results that have emerged from these experiments will be published separately and will be, then, only briefly evoked.

4.1. General Kinematics and Mechanical Model Behavior

In all our experiments, two main stages are always observed: a transient period of general elastic loading followed by a period characterized by stick-slip behavior.

During the loading stage, the fault is totally locked and the model starts recording long wavelength (>500 mm) elastic deformation. The mean duration of this stage depends on the loading rate but also on the imposed normal stress and fault friction properties. Generally, stick-slip behavior is observed along the fault plane after about 10 mm of bulk shearing.

During the second main stage, seismic cycle-like phases of deformation can be observed and measured. This phase is characterized by the occurrence of instantaneous incremental slip events separated by a few minutes during which the fault appears to be partially or totally locked. Figure 7 shows a short sequence, representing 2 mn of duration, extracted from a typical experiment monitored every 6 s. Interseismic loading, characterized by the absence of slip on the fault plane, dominates. Time to time, the fault gets unlocked and an incremental slip is generated (coseismic rupture). Main coseimic slip events are characterized by maximum horizontal amplitude displacements of 100 to 250 μm with rupture length varying from 600 to 900 mm and mean return periods of 30 to 180 s depending on the loading rate. The sequence presented in Figure 7 can be described as follows.

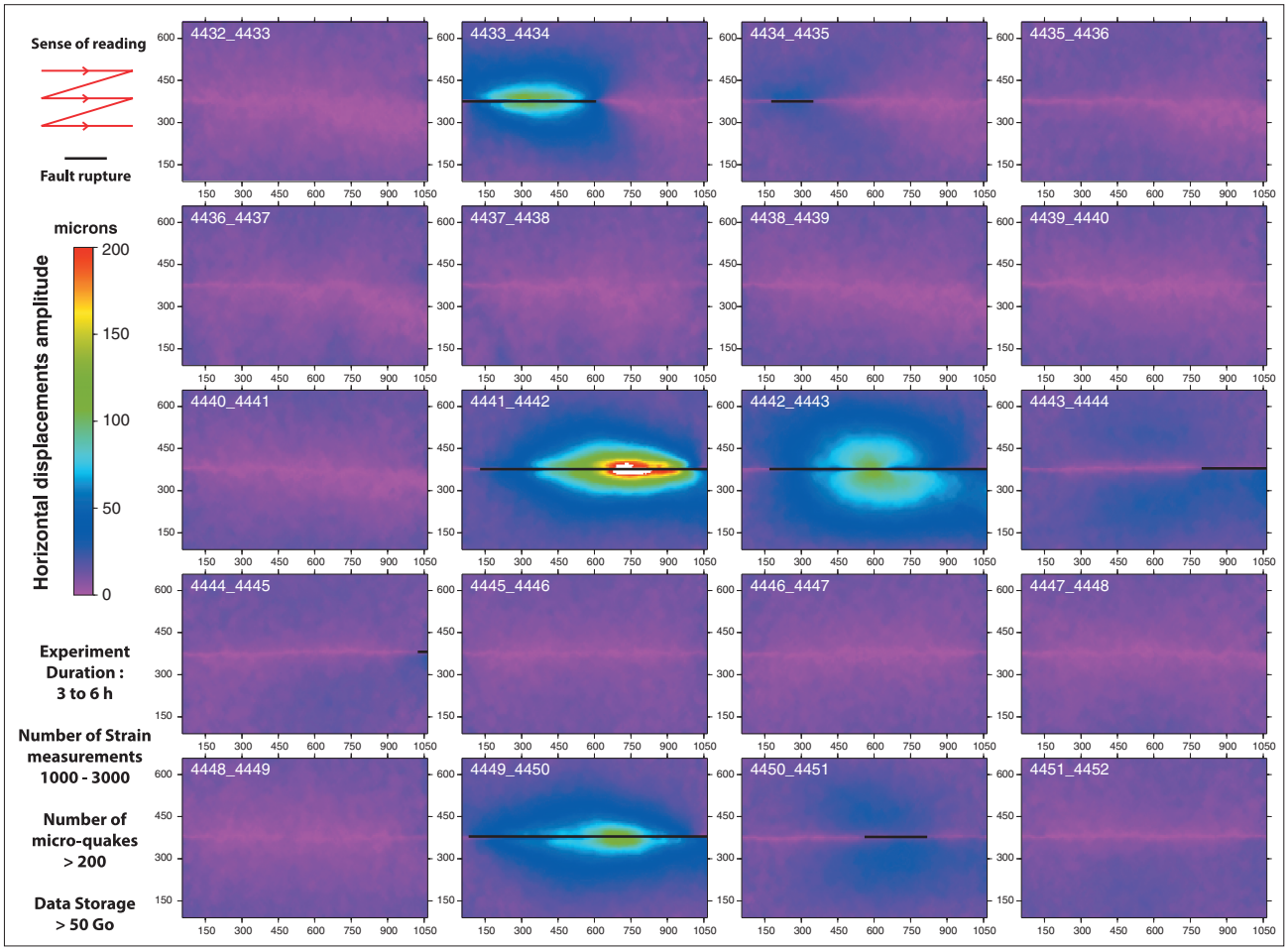

Figure 7. Examples of surface horizontal displacement measurements acquired during a typical experiment. Each stage is separated by 6 s corresponding to 20 μm of far-field simple shear model deformation. Stick-slip behavior is observed; instantaneous incremental fault slip events are separated by long time periods where the fault is locked and model records long wavelength elastic loading. Horizontal black lines indicate rupture locations along the fault trace.

After an interseismic phase of loading (P4432–4433, $t = 0$ s), during which the fault appears to be totally locked, a first microquake ruptures the left part of the fault over a length of 600 mm (P4433–4434, $t = +6$ s). Maximum coseismic surface slip of this event is in the range of 100–150 μm. Immediately after this coseismic stage, residual fault slip, located in the previous maximum coseismic slip area is observed (P4434-4435). Fault slip is concentrated over a length of about 150 mm. In the next six stages (from P4435–4436 to P4440–4441) the fault remains locked for a period of 36 s during which model experiences additional elastic loading.

At $t = +54$ s (P4441–4442) a second large microquake ruptures the central and right portion of the fault. It is characterized by a maximum surface coseismic slip of about 210 μm and rupture length of 900 mm. After this second coseismic phase, the fault still slips but with lower amplitude and the displacement pattern on the model surface is more widely distributed. (P4442–4443, $t = +60$ s).

On the stage (P4443–4444, $t = +66$ s), the part of the fault, that previously ruptured, shows no displacements indicating its relocking, whereas small motions are still visible in the far-field of both compartments.

The next interseismic phase (P4444–4445 to P4449–4450) lasts for 30 s during which the fault is again totally locked except for a very low magnitude slip event located on the right fault termination (P4444–4445).

At $t = +102$ s (P4450–4451), a third microquake ruptures the whole fault with a maximum coseismic surface slip of about 120 μm. It is followed, as for the first microquake, by a localized residual fault slip extending over a fault length of about 100 mm.

The fault locked again and a new interseismic phase starts (P4452–4453, $t = +120$ s). It is interesting to note that the postseismic phase characteristics depend on the microquake magnitude. For small to moderate coseismic events, only after-slip like deformation is observed rather for strong microquakes, off-fault displacements occur implying deep fault slip and, most probably, viscous deformation at the brittle-ductile transition.

Experiment duration depends on the imposed loading rate and typically ranges from 3 to 6 h. During that time, it is possible to generate and analyze hundreds of seismic cycles. In the experiment presented in Figure 7, the model generated more than 200 seismic cycles for a total cumulated slip on the fault of about 60 mm. This ratio is not constant and depends on several boundary conditions such as loading rate, initial normal stress and fault friction properties. The capability of the model to generate a great amount of successive seismic cycle is a key point of our approach because it allows performing parametric and statistical analysis that are almost impossible to realize on natural cases.

4.1.1. Interseismic Displacement Field

During the interseismic loading, the strain field is mostly characterized by the absence of measurable slip along the fault, which may indicate that the fault is totally locked. Punctually in space and time, episodic and local phases of low-velocity slip that can be interpreted as aseismic creep are also observed. Interestingly, fault-parallel horizontal displacement velocity v profiles across the fault can be adjusted by using the formulation proposed by *Savage and Burford* [1973]:

$$v(y) = \frac{v_0}{\pi} \arctan\left(\frac{y}{\mathrm{Dl}}\right) \tag{3}$$

with $v(y)$ the velocity at the distance y from the fault, V_o the far-field velocity (boundary or shearing velocity, relative plate motion), and Dl the locking depth. This formulation links the velocity of any point of the surface to its distance compared to the fault trace and to the depth limit of the locked portion of the fault which can be approximated as the brittle/ductile transition [*Weertman and Weertman*, 1964; *Savage and Burford*, 1973; *Savage*, 1980; *Lisowski*, 1991]. This 2-D model is often used to invert the slip rates and the locking depth of strike-slip fault [e.g., *Schmalzle et al*., 2006; *Titus et al*., 2011]. A typical experimental interseismic strain field and displacement profile is shown Figure 8c. The displacement amplitude and the vector field show that the central part of the fault is totally locked. The displacement increases symmetrically on each side from the fault toward the far field where it reaches the long-term imposed velocity loading. The velocity profile across this zone exhibits a typical arctangent shape that can be adjusted using equation (3). Results give a long-term boundary model velocity of 20 mm/h and a locking depth of 60 mm which correspond to the imposed loading rate and the foam thickness, respectively (Figure 8c). Figure 8d underlines the similarity with interseismic geodetic measurements across the San Andreas Fault (California, USA).

Figure 9 shows another example of interseismic model deformation where slow velocity fault slip (<60 μm/6 s) is observed. The velocity profile is nearly flat on both compartments indicating very low elastic loading. The velocity gradient across the fault is much higher here and shows a good analogy with measurements performed on natural cases (Figure 9d) such as across the creeping part of the North Anatolian Fault [e.g., *Cakir et al*., 2005]. This profile can be adjusted using a shallow locking depth of 7 mm and a long-term boundary model velocity of 13 mm/h, consistent with the imposed loading rate for this experiment (Figure 7c). Fault locking and fault creep behaviors can be seen as two end-members characterizing the interseismic phase. In our experiments, intermediate behaviors with partial coupling are often observed during the interseismic phase.

4.1.2. Coseismic Displacement Field

Recurrent instantaneous incremental slip equivalent to coseismic ruptures, separated by interseismic loading stages, are observed on the fault (Figure 10). In map view, horizontal surface displacements distribution forms an ellipse whose major axis is mingled with the fault trace (Figure 10a). Fault-perpendicular profile shows fault-parallel displacement reaching up to few hundreds of microns close to the fault with a rapid decay on both sides (Figure 10c). As noticed by *Reid* [1910] coseismic surface motions show the opposite pattern compare to interseismic surface motion. This observed displacement field can be successfully reproduced using classical elastic half-space dislocation models, which are commonly used to quantify coseismic displacements on active fault [e.g., *Steketee*, 1958a, 1958b; *Chinnery*, 1961; *Savage and Hastie*, 1966; *Savage and Burford*, 1973; *Okada*, 1985]. This simple model is based on the equation:

$$u(y) = \frac{u_0}{\pi} \arctan\left(\frac{D}{y}\right) \tag{4}$$

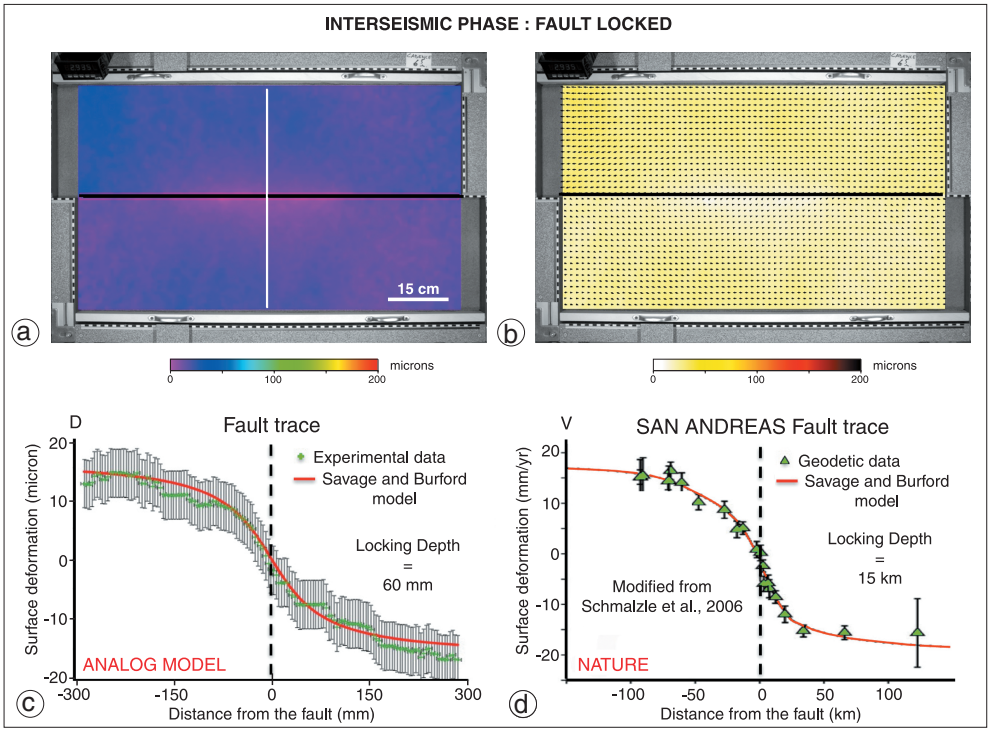

Figure 8. Example of an interseismic phase showing fault locking. (a) Amplitude of horizontal fault-parallel surface displacements. (b) Vector field superimposed on the amplitude of horizontal surface displacements. (c) Fault-perpendicular displacement profile showing the typical arctangent shape (green: experimental data and red: Savage and Burford model with a 60 mm locking depth). (d) Example of an interseismic velocity profile (horizontal GPS data) across the San Andreas Fault.

with U the horizontal surface displacement parallel to the fault at the distance y from the strike, U_0 the slip on the fault, and D the dislocation depth (Figure 10c).

For comparison, Figure 10d shows coseismic displacement profiles of the 1997, $M_w = 7.6$, Manyi earthquake [*Peltzer*, 1999]. The similarity between experimental and geodetic measurements confirms that model coseismic surface displacements are analog to those observed in natural fault systems.

On an energetic point of view, seismic moment can be calculated using the shear modulus of the crust (G), the rupture surface (S), and the mean coseismic slip along the fault plane (u) with the following relation:

$$M_0 = GSu \tag{5}$$

Base on the deep slip inversions on the fault plane detailed in section 4.2, typical large microquakes are usually characterized by a surface rupture of 0.7 m × 0.05 m and a mean coseismic slip of $u = 1.5 \times 10^{-4}$ m. Using model physical and mechanical parameters; a shear modulus $G = 45$ kPa and a fault surface $S = 0.035$ m^2, seismic moment (M_0Model) can be evaluated to about 2.4×10^{-1} N m. Using the average scaling factor L^*, the calculated earthquake equivalent source parameters correspond to a surface rupture of 175 km × 7.5 km and a mean coseismic slip $u = 25$ m. With an upscaled $G = 11$ GPa, the seismic moment (M_0Nature) is estimated to about 3×10^{20} N m, given a model to nature ratio of about 5.3×10^{-22}. Thus, such a large microquake in our experiments correspond to an earthquake magnitude $M_w = 7.7$. Note that in regards to earthquake scaling laws [*Wells and Coppersmith*, 1994] u appears to be overestimated with a factor of 5 considering the rupture dimensions. This point will be discussed later in section 5.

4.1.3. Postseismic Displacement Field

It is now well established that both after-slip and viscoelastic relaxation contribute significantly to postseismic deformation. After-slip is commonly associated with additional slow slip on the fault plane in the region surrounding the coseismic rupture area [e.g., *Thatcher*, 1983; *Li and Rice*, 1987; *Ben-Zion et al.*, 1993; *Scholz*, 1998; *Montési*, 2004], whereas viscoelastic rebound is attributed to viscous shearing nearby the

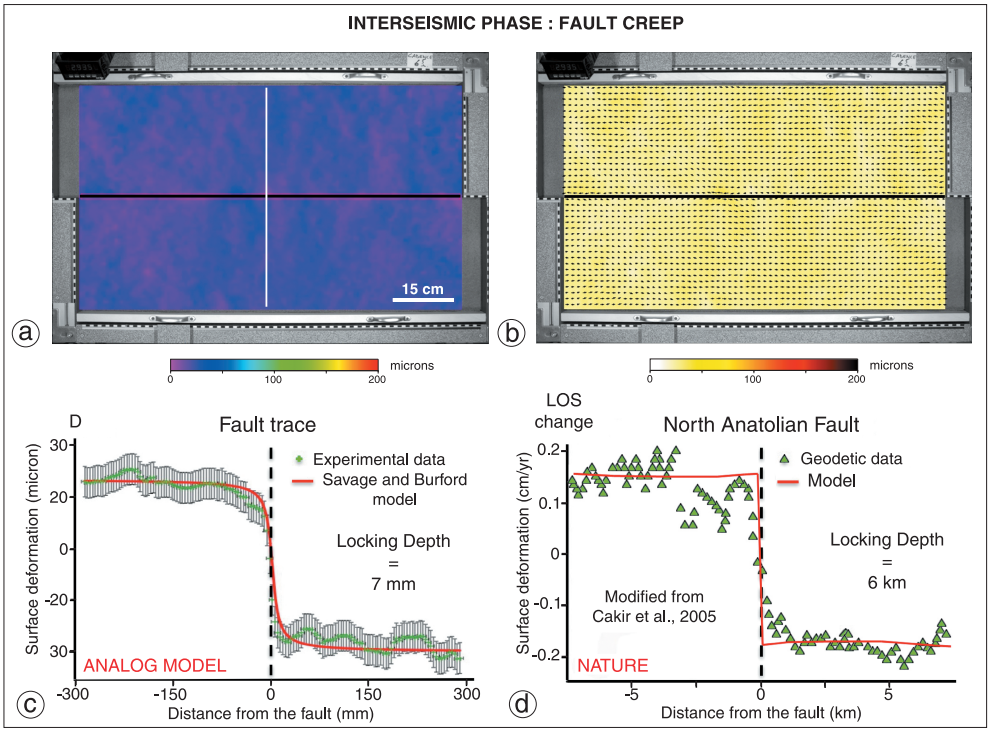

Figure 9. Example of an interseismic phase showing fault creep. (a) Amplitude of horizontal fault-parallel surface displacements. (b) Vector field superimposed on the amplitude of surface displacements. (c) Fault-perpendicular displacement profile showing the typical arctangent shape (green: experimental data and red: Savage and Burford model with a 7 mm locking depth). (d) Example of an interseismic velocity profile (InSAR data) across the North Anatolian Fault.

brittle/ductile transition in response to coseismic stress change [*Nur and Mavko*, 1974; *Pollitz et al*., 2001; *Fialko*, 2004a]. Postseismic deformation generally decays after a few days or months and eventually after several years for major earthquakes. In our modeling, immediately after the occurrence of major microquakes, surface displacement field exhibits two main features; fault creep, and low-amplitude long wavelength deformation (Figure 11). Slip along the fault trace may correspond either to the end of the coseismic rupture or to aseismic after-slip following the earthquake [*Smith and Wyss*, 1968; *Marone et al*., 1991; *Perfettini and Avouac*, 2007]. The two displacement maxima located off-fault on both compartments associated to a long wavelength deformation can be associated with deep slip controlled by viscous relaxation. Thus, as in natural cases, these features can be interpreted as the joint effect of fault slip and viscous deformation at the bottom of the model. Note that for experiments performed with a pure-elastic rheology, i.e., without the basal silicone layer, this postseismic phase of deformation is not observed. This confirms that the mechanical coupling at the interface between the polyurethane foam plates and the silicone layer play a key role in the relaxation of coseismic stress. Due to the sampling rate of the monitoring system (one measurement every 6 s), the postseismic phase can be identified during one or two pictures following the coseismic rupture. Typical relaxation time of the ductile layer is probably a little bit greater than 6 to 12 s because, due to monitoring accuracy and the rapid decay of postseismic deformation, its signal is lost before this phase ends. Furthermore, considering a viscosity $\eta \sim 50$ kPa s and a shear modulus $G \sim 3$ kPa [e.g., *Boutelier et al*., 2008] for the silicone layer, we calculate a Maxwell relaxation time $t \sim 16$ s (with $t = \eta/G$) consistent with the experimental measurements.

4.2. Microquake Characteristics

To characterize and compare the kinematical and mechanical properties of experimental microquakes to their natural counterparts, we have studied the relationships between several key parameters that are classically used to analyze earthquake dynamics [e.g., *Wells and Coppersmith*, 1994; *Manighetti et al*., 2005; *Wesnousky*, 2008]. Results are also used to evaluate and discuss model scaling.

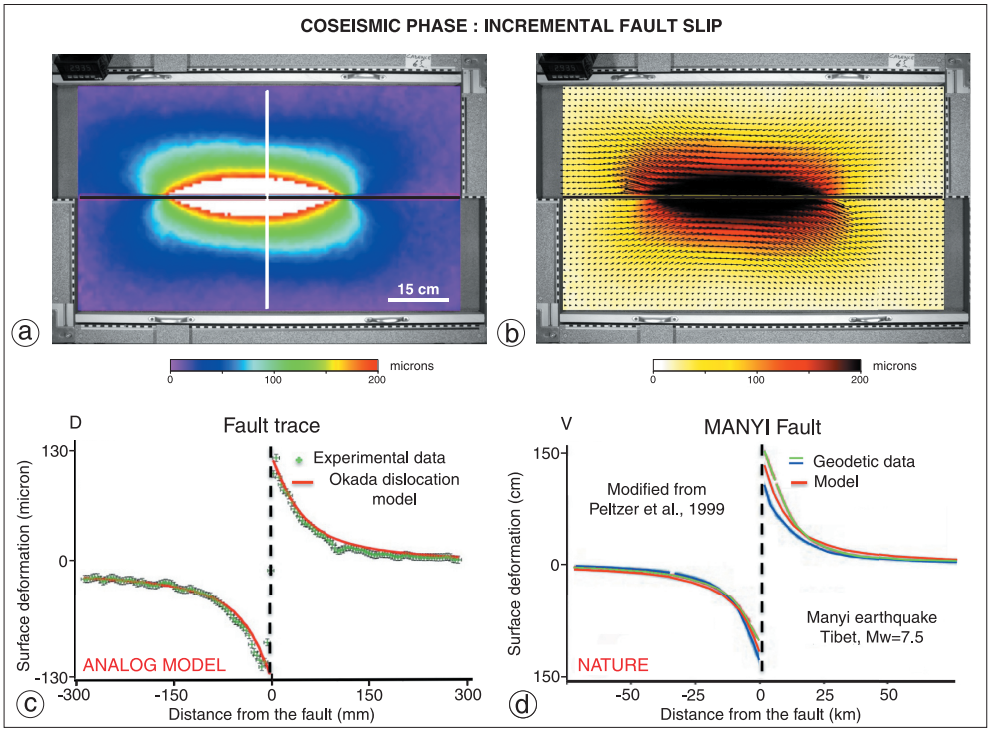

Figure 10. Example of a coseismic phase showing incremental fault slip. (a) Amplitude of horizontal fault-parallel surface displacements. (b) Vector field superimposed on the amplitude of surface displacements. (c) Fault-perpendicular displacement profile showing typical far-field attenuation of surface displacements (green: experimental data and red: Okada half-space elastic dislocation model). (d) Example of coseismic displacement profile (InSAR data) induced by the Manyi, $M_w = 7.6$, earthquake.

4.2.1. Surface Slip Profiles

The analysis of surface coseismic fault displacement profiles give interesting informations to better constrain rupture propagation mechanisms and fault growth processes. For that, we extracted the fault-parallel component of horizontal offsets along the fault. In several cases, the rupture tips of experimental microquakes cannot be determined precisely; especially when the microquake occurs near the model fault ends and when the microquake breaks the whole fault. In both cases, the apparent rupture length is shorter than the true length. To overcome this limitation, estimate true surface fault slip gradients and allow the comparison with natural cases, half-displacement profiles were considered as it is usually done to study the long-term and coseismic fault slip gradients [e.g., *Dawers and Anders*, 1995; *Cartwright and Mansfield*, 1998; *Soliva and Benedicto*, 2005].

Figure 12a shows a selection of 64 coseismic fault slip profiles (fault-parallel component of horizontal surface displacements). Fault creep events were removed from this selection by identifying slip events having average displacement lower or equal to the imposed interseismic far-field displacement. Half-displacement profiles are defined here as the displacement distribution from the location of the maximum rupture displacement (D_{max}) to the location of the rupture tip along the fault. They are normalized by the maximum rupture length and maximum fault displacement (D_{max}). In Figure 12, D_{max1} and D_{max2} refer to the difference between D_{max} and fault displacement at left and right rupture tips. $L1$ and $L2$ correspond to the left and right portions of the rupture length compare to D_{max} location.

Different types of profile geometry are observed. Some profiles exhibit a convex shape while others appear concave. At first order, all of these profiles can be reasonably adjusted using a linear fit, which implies that most of the fault displacement distributions are substantially triangular. Nevertheless, nonlinear profiles such as bell-shaped or flat-topped distributions are also observed, as well as profiles with multiple local maxima. These types of profiles shapes and especially the linear displacement distribution between D_{max} and the rupture tips are fully consistent with what it is observed in the nature [*Manighetti et al.*, 2005; *Wesnousky*,

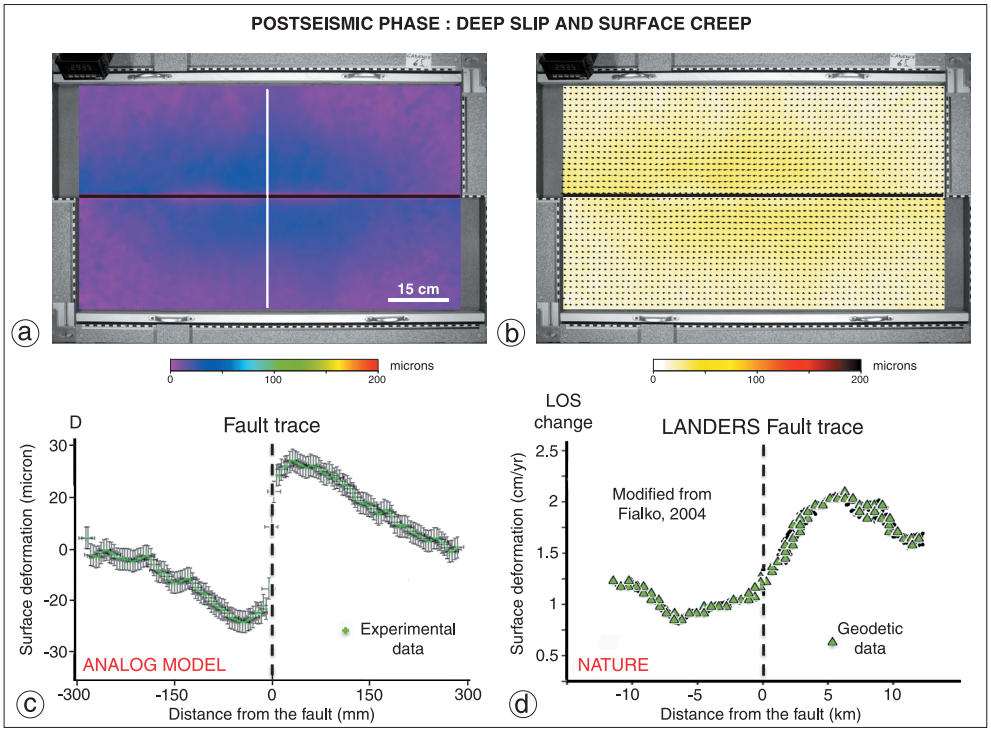

Figure 11. Example of a postseismic phase during which fault slip concentrates at depth near the brittle/ductile transition and close to the model surface. (a) Amplitude of horizontal surface displacements. (b) Vector field superimposed on the amplitude of horizontal surface displacements. (c) Fault-perpendicular displacement profile showing maximum surface displacements located away from the fault trace. (d) Example of a postseismic velocity profile (InSAR data) for the Landers earthquake.

2008]. The diversity of the profile shapes observed has also been modeled using mechanical analytical solutions or numerical models [e.g., *Bürgmann et al.*, 1994; *Willemse*, 1997].

4.2.2. D_{max} Versus D_{mean}

Figure 12b shows the relationship between D_{max} and D_{mean} (mean value of displacement) from the displacement profiles. D_{max} values appear to be ~1.7 greater than D_{mean} and the ratio $\gamma D = D_{max}/D_{mean}$ is constant. These two characteristics are very similar to those evidenced for natural strike-slip earthquakes [*Wells and Coppersmith*, 1994; *Manighetti et al.*, 2005, 2007; *Martel and Shacat*, 2006]. According to these studies, this γD ratio value is typical of near triangular shape slip profiles.

Elliptic slip profile shapes, predicted by elementary models for slip in a linear elastic homogeneous and isotropic material [*Pollard and Segall*, 1987], are never observed in our experiments. These theoretical slip distributions are characterized by infinite displacement gradients at fault tips inducing stress singularity. This unrealistic behavior is theoretically related to the finite dimension of the fault rupture in an elastic space and to the absence of both fault friction and heterogeneous damage inherent to fault zones, approximated in the form of cohesive end zones in mechanical models [*Dugdale*, 1960; *Scholz*, 2002]. In the near-linear distribution of displacement observed in the experimental microquakes (Figure 12a), tapers are observed at rupture ends and cannot be related to off-fault plastic damage surrounding the rupture, but probably more to on-fault processes. This implies specific properties of yield and driving stresses, expressed more simply by dynamic, static friction, and stress distribution near the fault tip [*Dugdale*, 1960; *Barenblatt*, 1962; *Kanninen and Popelar*, 1985; *Wang et al.*, 1995; *Bürgmann et al.*, 1994; *Willemse*, 1997].

Preliminary results strongly suggest that initial static normal stress distribution is a key parameter influencing significantly the location and displacement distribution of microquake events along the fault plane. Such a specific study would be presented in a forthcoming publication (Caniven et al., How along-fault stress heterogeneity controls seismic cycle fault behaviour? Insights from an experimental strike-slip fault model, submitted to *Tectonophysics*, 2015).

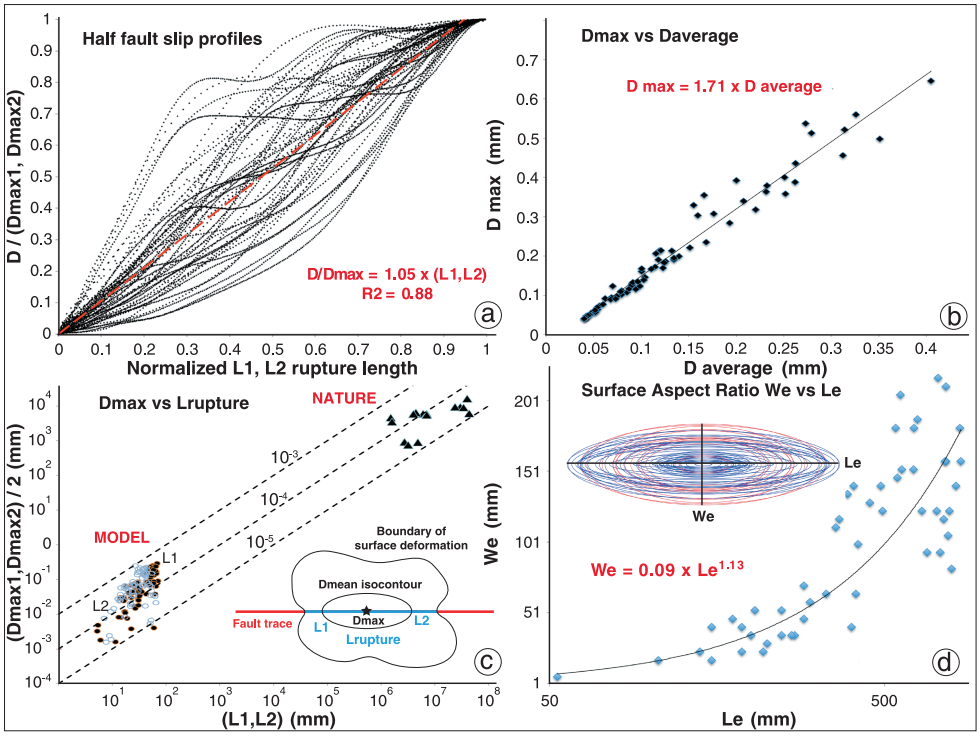

Figure 12. (a) Fault-parallel horizontal displacements vs normalized distance along the fault (half profiles). (b) Maximum displacement (D_{max}) versus average displacement (D_{mean}) from profiles of the graph (Figure 12a). (c) Half maximum fault-parallel displacements (D_{max1}, D_{max2}) versus half rupture length (*L1*,*L2*). Earthquakes data from *Wells and Coppersmith* [1994], *Manighetti et al.* [2005], and *Wesnousky* [2008]. (d) Surface displacements aspect ratio (*Sar*): major (Le) versus minor (We) axis of average displacement (D_{mean}) isocontour.

4.2.3. D_{max} Versus *Lrupture*

To study how surface fault slip evolves with different rupture length, we investigate the relationship between D_{max1}, D_{max2}, and *L*1, *L*2. Figure 12c shows that for experimental microquakes, the calculated ratio $\gamma co = D_{max1,2}/L_{1,2}$ typically ranges between 10^{-5} and 10^{-3} which is very close to that of natural earthquakes [*Wells and Coppersmith*, 1994; *Manighetti et al.*, 2005; *Kim and Sanderson*, 2005; *Wesnousky*, 2008]. Nevertheless, we note that stronger slip events tend to have higher γco than natural earthquakes. This discrepancy is probably related to the finite dimension of model's fault which is not long enough. The low-friction patches at the fault tips act as barriers to the seismic rupture propagation which induce strong coseismic slip gradients when the whole fault is broken.

4.2.4. We Versus Le

Finally, we analyze the pattern geometry of coseismic surface deformations produced in the vicinity of the fault rupture. Interest is to study the relation between fault slip kinematics along the fault plane and large-scale model deformation. As expected from elementary mechanics in elastic medium [*Chinnery*, 1961], fault-parallel surface displacement contours evolve progressively from an ellipse near the observed maximum surface slip to a butterfly shape away from the fault rupture (as seen in Figure 10a). To measure and compare microquakes surface aspect ratio (Sar) with nature, we extract the mean horizontal displacement isocontour on an interval delimited by the interseismic and the maximum fault slip values. From obtained elliptical isocontour, a major (Le) and a minor (We) axis can be extracted (Figure 12d). The Sar ratio, i.e., *(*Le*/*We*)*, varies from 2 to 10. Although the dispersion is high, (We) seems to increase following a power law, with $a\ x\ (Le)^b$. Here the regression gives $b = 1.13$ with a $R^2 = 0.75$, (the law is linear and the ellipse considered self-similar for $b = 1$).

The dispersion of data and the plot of all ellipses obtained from measured (We) and (Le) suggest that, at least, two main types of events could be distinguished: (1) microquakes with a Sar < 4 (red ellipses on Figure 12d) that are related to single-slip events such as the one shown in Figure 10a with "bell-shaped" slip

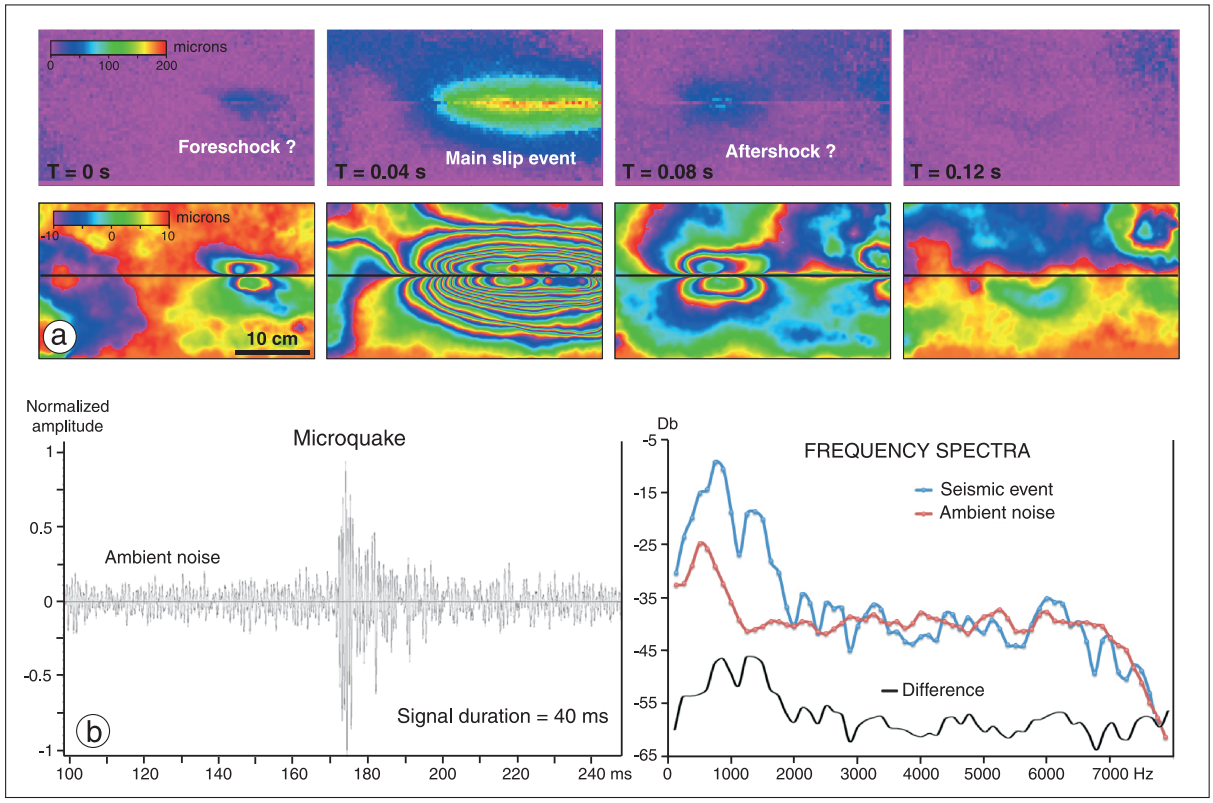

Figure 13. (a) First results obtained during the experiment with a standard HD camera taking 25 images/s. Amplitude of horizontal surface displacements (top) and associated synthetic interferogram (bottom) are presented. Each stage is separated by 1/25 s. At this sampling frequency, the propagation of the rupture is not visible but it is possible to detect seismic events that occurred just prior and after the main shock which could be interpreted as foreshocks and aftershocks. (b) Example of acoustic record (left) of a strong microquake with piezoceramic sensors (resonance frequency 4400 Hz) and its associated frequency spectra (right, blue curve). The red curve is the ambient noise frequency spectra. The black curve indicates the difference between the red and the blue curves. Db: decibel.

profiles and (2) microquakes with a Sar >4 (blue ellipses in Figure 12d) that could be the result of the addition of several-slip events, flat-topped or heterogenous coseismic slip distributions.

For natural earthquakes, the Sar ratio is not directly studied. Nevertheless, based on some examples of coseismic surface deformation derived from geodetic measurements (optical subpixel correlation and InSAR) [*Wang et al.*, 2007; *Qu et al.*, 2013; *Avouac et al.*, 2014], Sar seems to increase with the magnitude [e.g., Yushu earthquake, 2010, *M* 7.1, Sar~3; Balochistan earthquake, 2013, *M* 7.7, Sar~6].

As coseismic surface displacements are related to the fault slip at depth, Sar can be compare to the more classical aspect ratio defined by *L*/*W*, with *L* the surface rupture length and *W* the rupture width (in depth). For natural strike-slip earthquakes, although *W* is quite constant in a small range related to the seismogenic continental crust depth (10–15 km), higher *L* of strong earthquakes tend to be associated with large *W* [*Wesnousky*, 2008].

4.2.5. Microquake Duration

The sampling frequency of 0.17 Hz (one acquisition every 6 s) used for optical measurements does not permit to estimate the real duration of the coseismic phase. By using a standard high-definition (HD) digital camera, recording 25 images per second, we have quantified that experimental microquake duration generally does not exceed 50–100 ms, implying coseismic rupture velocities of about a few tens of meters per second and coseismic slip velocities in the range of 0.02–0.04 m s (Figure 13). At this sample rate (25 Hz), we have been able also to capture some interesting additional details of the coseismic phase as illustrated in Figure 13a. After an interseismic loading phase which lasted for several minutes, one first small magnitude slip event is detected. It is followed, 1/25 s later, by a large slip event shearing the same maximum slip location. In the next 1/25 s, two additional slip events microquakes with small magnitudes occurred close to the rupture ends of the main event (Figure 13a). Taking into account the characteristics of this sequence

and particularly the fact they occur at different apparent slip rates, these seismic events could be interpreted as foreshock, main shock, and aftershock sequences, even if the hypothesis of a single-event propagation cannot be excluded considering the 25 Hz measurement sampling rate. Note that this experiment has been performed without the silicone layer at the base of foam plates, which explain the absence of the postseismic deformation phase (at $T = 0.12$ s), that is detected in foam/silicone models (Figure 11).

Additionally, microquake duration has been confirmed using vibration sensors (piezoceramic transductor, resonance frequency 4400 Hz), installed nearby the fault at the surface of the model (Figure 13b).

More interestingly this data reveals a complex signature that could be analyzed in future studies to derive information about the seismic source.

4.2.6. Coseismic and Interseismic Strain and Stress Fields

Model strain and stress state evolution can be studied in detail using the large catalog of surface displacements. This is of great interest to better understand how long-term stress-loading influence short-term stress evolution (i.e., at the scale of one seismic cycle) and also to investigate stress transfer processes with the aims to constrain the location and size of the future rupture events.

Because the vertical component of surface displacements is not measured, it is not considered in the following calculations. This is not a limiting factor since the fault has a pure strike-slip kinematics and, as shown by elastic dislocation modeling [*Okada*, 1985], vertical displacements are at least 1 order of magnitude smaller than horizontal displacements. Thus, plane strain conditions (2-D) are assumed and the components of model surface strain and stress tensors are, then, derived from the horizontal surface displacements using the following formulations:

$$\varepsilon_{xx} = \frac{\partial u}{\partial x};\ \varepsilon_{yy} = \frac{\partial v}{\partial y};\ \varepsilon_{xy} = \frac{1}{2}\left(\frac{\partial u}{\partial y} + \frac{\partial v}{\partial x}\right) \tag{6}$$

where the directions x and y and the displacements u and v are parallel and perpendicular to the fault, respectively. Next assuming linear elasticity, stress tensor σ is obtained from the Hooke's law

$$\sigma_{ij} = 2G\varepsilon_{ij} + \lambda\varphi\Delta_{ij} \tag{7}$$

with φ the first invariant of strain tensor, Δ the Kronecher's delta, and G and λ, the shear modulus and Lamé coefficient, respectively. By convention, compression and left-lateral sense are negative. An increase of shear stress value therefore indicates elastic relaxation, generally induced by a coseismic rupture or a creep event along the fault surface. The state of stress can also be specified with σ_1 and σ_2, defined as the maximum and minimum principal stresses, respectively. Their orientations relative to the fault trace is characterized by θ_1, the angle between x and σ_1. From the Cauchy's equations of the Mohr circle we have:

$$\sigma_{1,2} = \frac{\sigma_{xx} + \sigma_{yy}}{2} \pm \sqrt{\left(\frac{\sigma_{xx} - \sigma_{yy}}{2}\right)^2 + {\tau_{xy}}^2} \tag{8}$$

Because microquake displacements are heterogeneous, they generate stress heterogeneities along the fault plane: slipped zones are relaxed, whereas locked zone are loaded. This failure potential may be evaluated by using the Coulomb stress change criterion [e.g., *King et al*., 1994] defined as

$$\Delta\sigma_{\mathrm{cfs}} = \Delta\tau - \Delta\sigma_n.\mu \tag{9}$$

with u the effective static friction coefficient [*Jaeger and Cook*, 1979]. The fault being parallel to the X axis, for a slip event, the Coulomb stress change for optimally oriented vertical plane, [*King et al*., 1994, equation (13)] is defined by:

$$\Delta\sigma_{cfs} = \Delta\tau_{xy} - \Delta\sigma_{yy}.\mu \tag{10}$$

with $\Delta\tau_{\xi\psi}$ and $\Delta\sigma_{yy}$ the shear stress change and the normal stress change, respectively. Positive values of $\Delta\sigma_{\mathrm{cfs}}$ indicate an increase of Coulomb stress that promote failure, whereas negative ones promote a relaxation.

Figure 14 shows coseismic and interseismic strain and stress changes calculated from the cumulated displacement field between two consecutive measurements (12 s). During the interseismic phase (Figure 14a), the shear stress change component shows, as expected, a typical generalized elastic loading around the fault trace (Figure 14a2). For the considered time interval, we deduce a loading rate of about 1 Pa/s when and where the fault is locked. At the vicinity of locked patches (i.e., without creep), we can

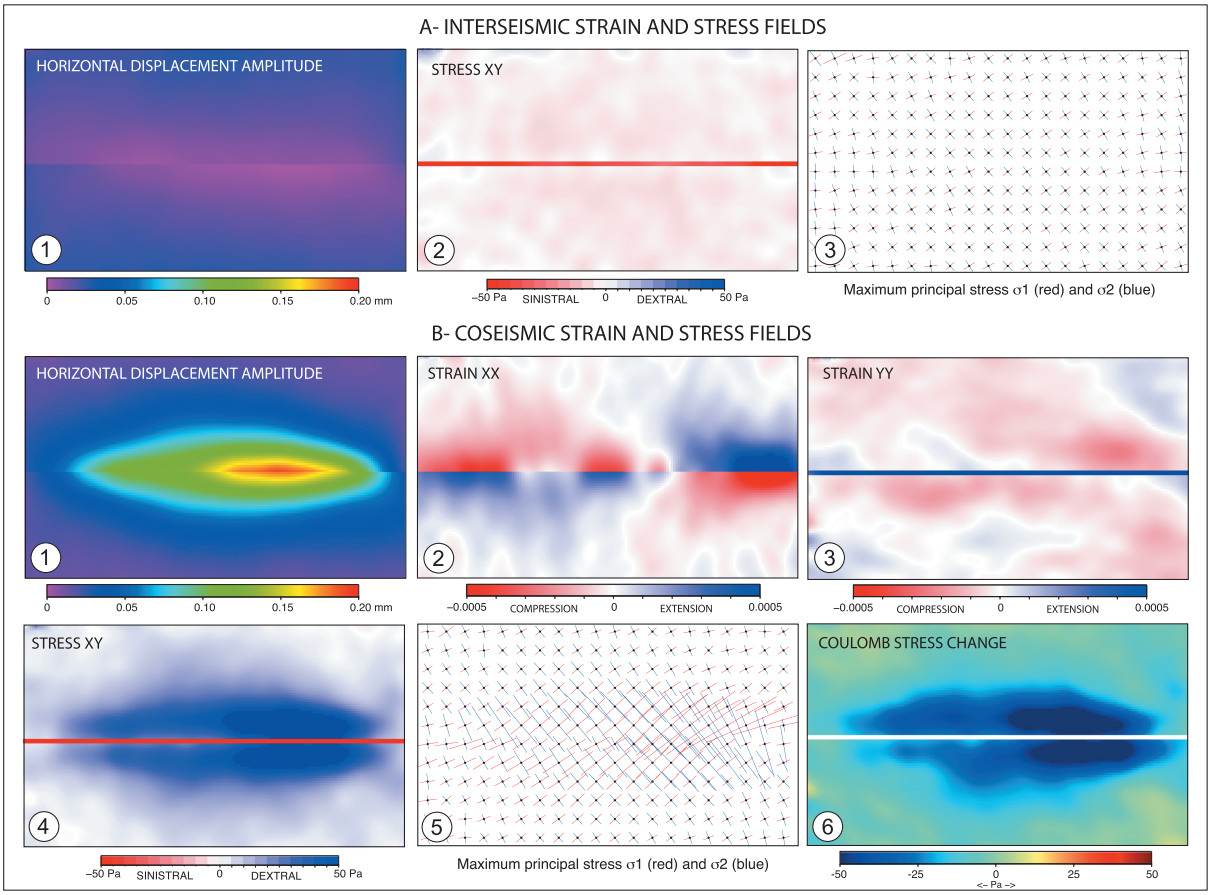

Figure 14. Examples of (a) interseismic and (b) coseismic surface strain and stress fields. Figure 14a1 shows the amplitude of interseismic horizontal displacements. Figure 14a2 shows the *XY* component of interseismic stress field. Figure 14a3 shows maximum principal components of interseismic stress (σ_1 in red and σ_2 in blue). Figure 14b1 shows the amplitude of coseismic horizontal displacements. Figure 14b2 shows the *XX* component of coseismic stress field. Figure 14b3 shows the *YY* component of coseismic stress field. Figure 14b4 shows the *XY* component of coseismic stress field. Figure 14b5 shows the maximum principal components of interseismic stress (σ_1 in red and σ_2 in blue). Figure 14b5 shows the coseismic Coulomb stress change.

reasonably consider that we measure the maximum-global stress-loading rate. The slight relaxation observed on both model fault tips are related to the presence of the low-friction patches, which prevent fault end locking as explained earlier in section 3.3.

The oblique orientation of the major principal stress σ_1 is coherent with the sinistral loading of the model (Figure 14a3), with an average θ_1 of 40° in the central part of the model. Effect of the low-friction patches is visible at fault ends, where σ_1 tends to parallel to the fault strike. Most of σ_2 values are negatives and have the same amplitude than σ_1 values, indicating that the principal stresses in the system balanced during the loading phase.

Due to low camera sampling rate (1 frame/6 s), these measurements include a part of interseismic and/or postseismic displacements. However, as coseismic displacements (Figure 14b1) are much higher by about one order of amplitude, we consider that most of the stress changes at this time scale results from the slip rupture on the fault plane. This is confirmed by the *XX* components strain map that clearly shows extensive and compressive quadrants, consistent with a sinistral slip on the fault (Figure 14b2). For this example, three mains lobe pairs can be distinguished which may indicate the occurrence of two separated microquakes or a single one with a heterogenous slip distribution.

The *YY* component of coseismic strain field (Figure 14b3) shows an unexpected heterogeneous asymmetric pattern compared to the theoretical strain/stress field in a homogeneous half-space elastic media [e.g., *Chinnery*, 1963; *Segall and Pollard*, 1980]. This discrepancy may be due to (1) a heterogeneous slip distribution on the fault plane associated to tapering of slip profiles near rupture ends, (2) the low amplitude of *v*

displacements (normal to the fault strike direction) which is close to measurement accuracy (~5–10 μm) and therefore badly constrained. In contrast, both stress and strain fields in their shear component (*XY*, Figure 14b4) show clearly a stress drop along the ruptured portion of the fault with a maximum value of 50 ± 5 Pa, located where the coseismic displacement is maximum. Consistently, with expected theoretical results [e.g., *Segall and Pollard*, 1980] the perturbation of the principal stresses (Figure 14b5) indicates an increase of σ_1 (compression) and a decrease of σ_2 to negative values (tension) near the fault trace in the zone of maximum surface slip. The orientations of σ_1 axes are still consistent with the sense of fault slip [*Petit and Barquins*, 1988].

The Coulomb stress change associated to this coseismic event using equation(10) (Figure 14b6) is calculated considering a static friction coefficient of 0.65 ± 0.2 (see section 3.3). The isostress-change contours indicate a relaxation along the rupture zone with a pattern very similar to the shear stress field (Figure 14b4). This similarity is related to the very low coseismic normal stress change shown in Figure 14b3. We note that usually, stress lobes appear more pronounced for theoretical models with uniform slip along the dislocation [*King et al*., 1994]. Here the absence of pronounced positive lobes is attributed to the heterogeneity of slip and the low displacement gradient (taper) at the rupture tips. Another possible explanation is that a portion of postseismic after-slip is integrated in the analyzed measures and contributes to smooth the displacement distribution at both rupture ends.

Surface strain and stress fields, calculated from the horizontal displacement field, are consistent with expected interseismic and coseismic models [*Chinnery*, 1963; *Stein et al*., 1997; *Nalbant and McCloskey*, 2011]. Periods of quiescence produce large-scale stress loading whereas incremental slip events induce (1) local stress relaxation along the ruptured parts of the fault and (2) stress loading near both rupture tips. Stress changes induced by the last seismic cycles can be used to constrain the place and time of the next seismic event. On natural examples such data of regional and local stress perturbations around active faults are mostly unavailable.

4.2.7. Slip Distribution and Stress at Depth

To quantify the slip distribution at depth, we have developed a semi-automated inversion method, based on triangular dislocation elements embedded in a homogeneous elastic half-space [*Meade*, 2007]. The traditional approaches used a uniform small gridding for the fault plane [e.g., *Fialko*, 2004b]. Because of the limited number of observations, this gridding often leads to an underdetermined inverse problem, which is stabilized by smoothing slip model. While the small-scale surface displacements can be model with these approaches, the poorly resolved area can cause artifacts in the obtained slip distribution [*Page et al*., 2009]. In fact, this type of fault subdivision does not account for data coverage: patches located at depth or in areas that are sparsely covered by measurement are often poorly resolved.

Here following previous efforts [*Page et al*., 2009; *Atzori and Antonioli*, 2011], we favor the use of a nonuniform grid, which insures a homogeneous resolution. First, using the MATLAB MESH2D tool developed by D. Engwirda, we improve the model resolution by making the subfaults larger in poorly resolved area. The final model counts about 1000 dislocation elements. Patches near the edges and the bottom of the device have a size twice as large as those located at the top of the fault. Furthermore, we use an additional semiinfinite rectangular dislocation below the fault to simulate viscoelastic behavior and velocity boundary conditions. Next, with the MATLAB LSQLIN function, we inverse surface displacements constraining the sense of strike slip [*Coleman and Li*, 1996]. Because model parameters are all well known and the spatial resolution of surface measurements is very high, the results of the inversion are supposed well constrained. Figure 15 presents interesting preliminary results for four successive stages of model deformation corresponding to interseismic loading, coseismic slip, postseismic afterslip phase, and postseismic viscoelastic for a strong microquake event rupturing the whole fault.

Results of slip inversion suggest that during the interseismic phase, the fault is totally locked. Coseismic period is characterized by fault slips mainly located in the upper part of the fault. The obtained coseismic distribution gives about 0.5 mm for the maximum of slip located at 15 mm depth (Figure 15b), leading to an average Coulomb stress decrease of 100 Pa (Figure 15c). This value is consistent with surface estimate presented in the previous paragraph. Furthermore, our results predict a Coulomb stress increase in the lower part of the fault, where afterslip and deep postseismic are imaged in the 12 s following the event (Figures 15d and 15e). Slip affects the whole fault during the first phase of postseismic stage but with maximum values located deeper,

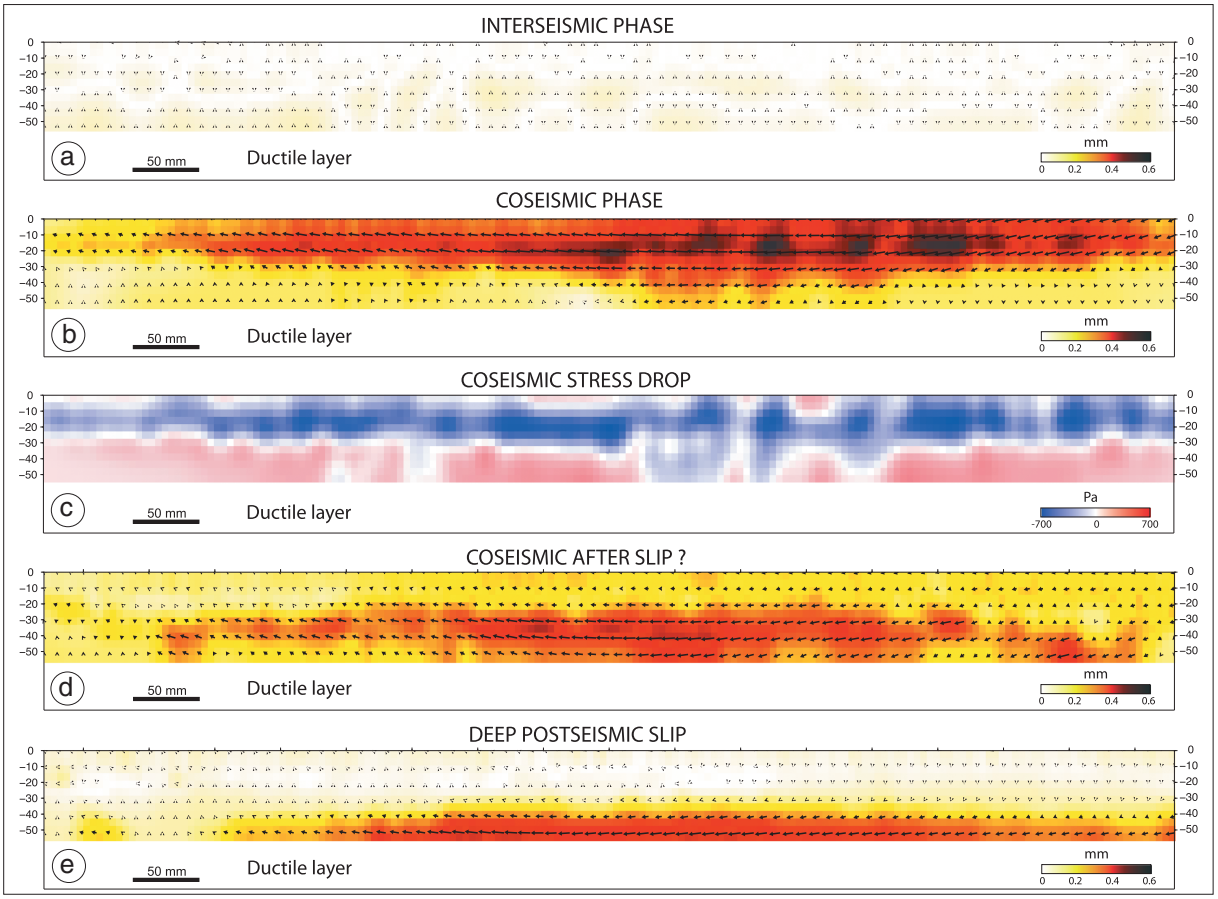

Figure 15. Results of fault slip inversion of four successive stages of model evolution. (a) Interseismic phase; the fault appears totally locked. (b) Coseismic phase; slip locates mainly in the upper part of the fault plane. (c) Associated Coulomb stress drop (mean stress variation of about −100 Pa). (d) Coseismic after slip phase; slip is concentrated in the middle to lower part of the fault plane. (e) Postseismic phase; fault slip is limited to the very lower part of the fault plane, near the brittle/ductile transition.

at 40 mm (Figure 15d). The following phase shows that slip is constricted close to the maximum depth of the elastic part of the model (Figure 15e). The fault is again locked in the upper central part. Some slight slips still persists at the surface and at the fault limits. This sequence shows a deepening of slip during the postseismic phase which can be compared to slip inversion results performed to study the $M_w = 7.5$ 1999 Izmit earthquake [*Reilinger et al.*, 2000]. In this case, coseismic slip was confined to the upper 10 km of the fault plane then evolve in the next month into aseismic afterslip located on and below the coseismic rupture.

This encouraging results point out the need to better constrain the effect of rheology, friction, and inherited stress on the obtained slip distribution at depth. However, this would request a systematic analysis that is beyond the scope of the present paper.

4.3. Seismic Cycle Characteristics

For each experiment, several hundreds of seismic cycles can be analyzed to study how the different deformation phases follow each others and what are the coupling processes that control their kinematics and mechanics characteristics. Several mechanical behaviors, analog to those evidenced in nature, can be identified and studied.

4.3.1. Clustering Behavior

In most of the 51 experiments that were performed, progressive rupture of the whole fault by successive microquakes is observed. Figure 16 shows a typical sequence of four successive microquakes rupturing the fault in a limited time (18 s, equal to ~ 200 years) after a long quiescence interseismic period of more than 180 s (equal to ~ 2000 years). In this sequence, microquake propagation appears unidirectional (from right

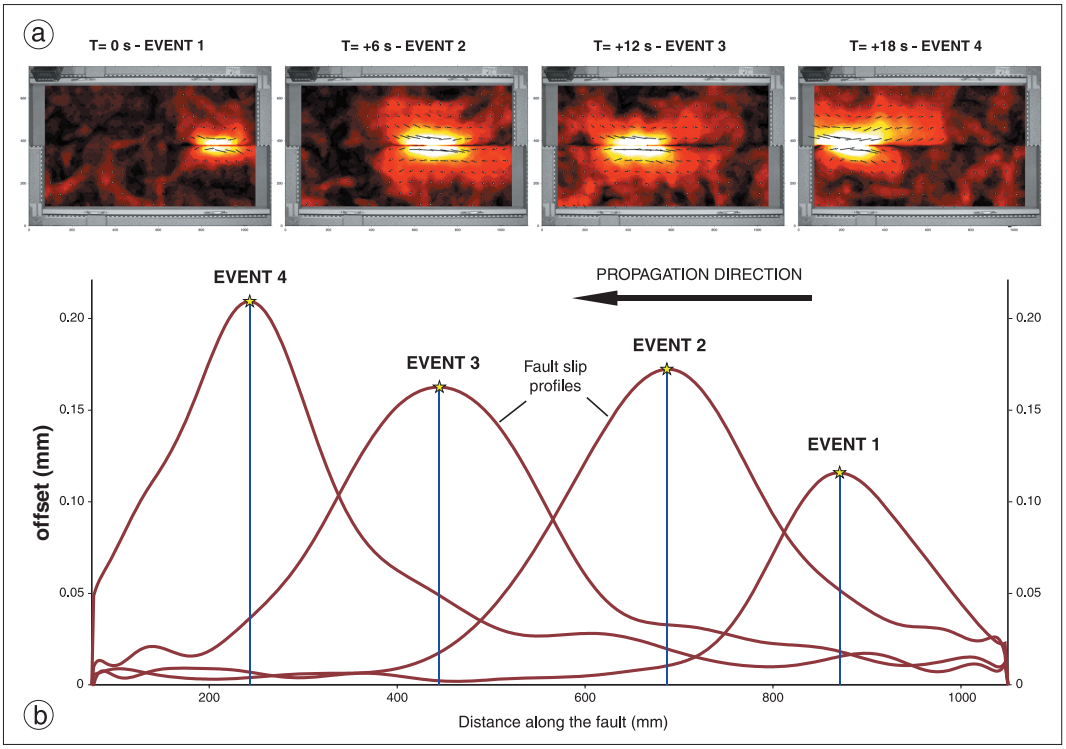

Figure 16. Example of microquake clustering. (a) Amplitude of horizontal surface displacements showing the progressive rupture of the fault by four successive microquakes propagating from right to left. (b) Associated horizontal fault slip profiles. Note that fault slip profiles are characterized by "Gaussian-like" or "bell-like" shapes.

to left) but bidirectional or even aleatory microquake clustering is also observed during the same experiment. It is not yet clear what are the parameters that control these behaviors but according to preliminary results, the initial normal stress distribution along the fault plane could plays a key role (Caniven et al., manuscript in preparation, 2014). It is interesting to note that microquake clustering seems inhibited in experiments where the amplitudes of normal stress variations along the strike are significants (>300 Pa). For the presented sequence, normal stress variations are less than 100 Pa, thus implying a uniform loading along the fault strike which seems to favor clustering behavior.

Earthquake clustering is commonly observed on natural fault like the North Anatolian Fault (NAF) for which several historical ruptures sequences have been documented [e.g., *Barka*, 1996; *Stein et al*., 1997; *Nalbant et al*., 1998]. The most famous is the 1939–1999 westward propagating sequence which ruptured ~1000 km of the NAF during eight major earthquakes, the last being the 17 August 1999 Izmit earthquake. In the last centuries, eastward propagating sequences has been also evidenced on the NAF [*Ambraseys and Finkel*, 1995; *Ikeda et al*., 1991; *Barka*, 1992] as well isolated events [e.g., *Pondard et al*., 2007]. Based on the analyses of stress transfers, *Pondard et al*. [2007] concluded that earthquakes clustering could be favored by a uniform loading along relatively linear fault segments. On the contrary, isolated events could be the consequence of nonuniform stress relief induced by previous earthquake sequences. That seems to be consistent with our observations concerning the role of normal stress distribution along the fault model.

4.3.2. Seismic Cycle Duration

For natural case studies, the evaluation of earthquake recurrence time period highly depends on several parameters like the time window of interest, the type of used data (geodetic, seismologic, and paleoseismologic), or even the location of the studied area along the fault. Experimentally, it becomes possible to access the complete model kinematics at any location and, then, constrain fault slip behavior at the scale of one seismic cycle up to long-term evolution. This analysis is also used to evaluate the kinematics and temporal scaling of the model.

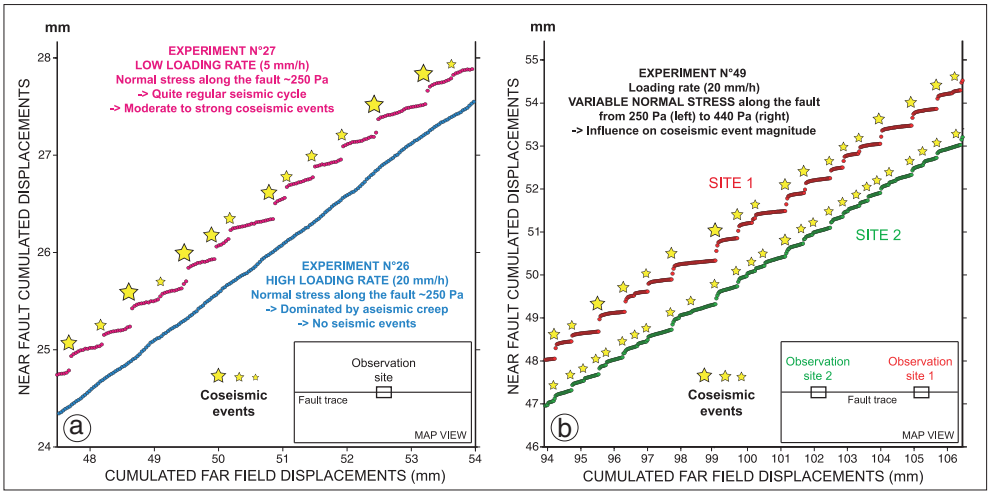

Figure 17. Evolution of cumulated horizontal surface displacements. (a) At one site near the center of the fault trace for two experiments performed with different loading rates of 5 mm/h (purple) and 20 mm/h (blue). Both curves are voluntarily offset from one another for easy reading. (b) At two sites along the fault for one experiment. Site locations are indicated by the sketch (bottom right). Normal stress at the site 1 (red) is about 440 Pa. Normal stress at the site 2 (green) is about 250 Pa. Both curves are voluntarily offset from one another for easy reading. *X* axis represents the far-field displacements.

Figure 17a illustrates different long-term faults slip behaviors by comparing the evolution of cumulated horizontal displacement at one site, situated close to the fault trace, for two experiments sharing the same parameters but performed with different loading rates. The observation site simulates a long-term GPS station implemented on one fault compartment. For this experiment, the average normal stress is about 250 Pa and is quite constant along the fault trace.

For a low loading rate (5 mm/h), the kinematics of the fault is characterized by the occurrence of strong and moderate microquakes with average surface slip of 250 μm and 80 μm, respectively. It is interesting to note that cumulated horizontal displacement slightly increases before most of major events implying that the fault unlock progressively until the fault breaks. This behavior is particularly observed for low loading rate (5 mm/h) experiments (Figure 17a). Then, due to postseismic viscoelastic relaxation, the slip rate decreases nonlinearly during a few tens of seconds.

The interseismic periods are characterized by a progressive increase of the cumulated displacements, meaning that the fault never locked totally and aseismic creep is occurring. Consequently, a significant part of model elastic loading is dissipated during the interseismic period. The average duration of these phases is ~ 300 s (4500 years). Note that interseimic locking of the fault is observed for low loading rate experiments when initial normal stress is higher. Coseismic displacements and recurrence times appears then more regular, close to a time and slip predictable seismic cycle [*Schwartz and Coppersmith*, 1984].

For a higher loading rate experiment (20 mm/h), aseismic creep dominates the fault slip behavior. Some creep rate variations are observed but the average velocity remains equivalent to the long-term slip rate. This feature indicates that the fault is almost unlocked and stores very little elastic energy. In a forthcoming study, we propose that this difference of fault behavior is most probably controlled by the brittle/ductile coupling at the base of foam plates, due to the strain-rate-dependent rheology of the silicone. For a high loading rate, viscous forces in the silicone layer increase as well as the mechanical coupling at the base of the foam plates which force the base of the frictional fault plane to slip at a velocity close to the far-field velocity. For a low loading rate, silicone almost behaves as a Newtonian fluid and viscous forces decrease significantly, allowing the fault to remain locked for a longer period. Another hypothesis is that a part of this behavior may be also controlled by a time-dependent static frictional strength [*Dieterich*, 1972, 1992; *Scholz* 1998; *Marone*, 1998]. Nevertheless, first results seem to favor the first hypothesis as the main process.

Figure 17b shows the same type of analysis but this time at two different sites along the fault for the same experiment. Site 1 and site 2 are located on the right and left portions of the fault, where normal stress is

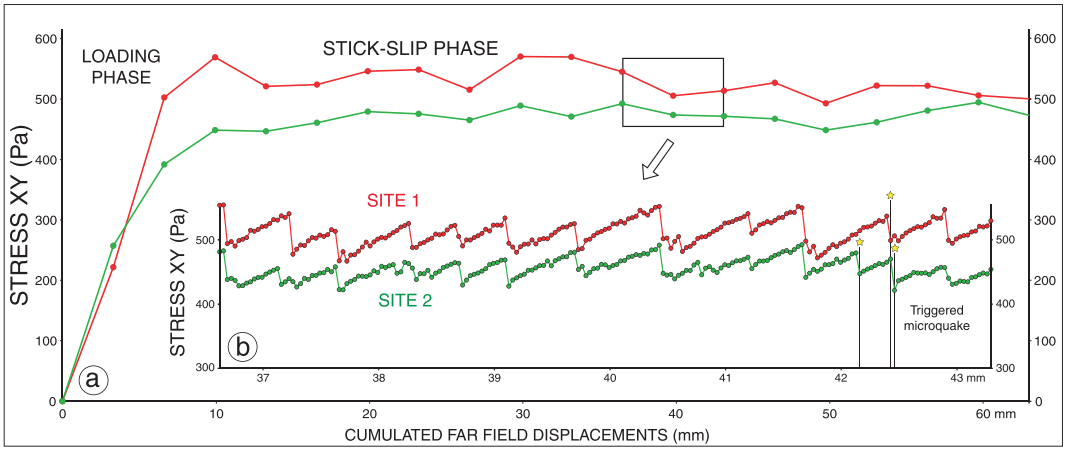

Figure 18. Cumulated *XY* shear stress component at two locations along the fault (same sites as for Figure 17b). Normal stress at site 1 (red) is about 520 Pa. Normal stress at site 2 (green) is about 450 Pa. (a) Long-term evolution is plotted using a measure sampling rate of 0.002 Hz. (b) Short-term (zoom) is obtained with a sampling rate of 0.17 Hz. Abscise axes represent the photo numbers, with 1 photo interval = 6 s.

440 Pa and 250 Pa, respectively. Due to these along-strike variations of the normal stress and resulting local changes in frictional strength, fault creep, or coseismic rupture can be locally enhanced or inhibited. Comparison between site 1 and site 2 measurements reveal that most of the major microquakes ruptured a long portion of the fault and are detectable on both sites, whereas smaller events affect generally only one site. Site 1 clearly records stronger slip events with a relative regular mean recurrence time of ~100 s (1500 years). At site 2, numerous smaller microquakes are observed, as well as significant interseismic creep. Average recurrence time at site 2 appears also shorter compare to site 1, about ~30 s (450 years). Fault slip appears, then, to be characteristics on site 1 while it is more chaotic on site 2.

This experiment illustrates the role of the normal stress distribution along the fault plane on sesimic cycle characteristics. It points out also the difficulty to constrain the complex and multiscale seismic behavior of active fault that arise when only local paleoearthquakes studies are considered [*Grant and Sieh*, 1994; *Sieh et al*., 2008; *Schlagenhauf et al*., 2011; *Goldfinger et al*., 2013].

4.3.3. Strain and Stress Evolution

As evoked earlier, one of the major interests of the experimental approach is to access the complete evolution of surface strain and stress fields, with their absolute values, from the beginning of the experiment. This analysis is also of interest to better constrain model scaling in term of mechanics and energy. Figure 18a illustrates how the *XY* component of surface stress evolves at two different sites along the fault during a typical experiment. Long-term shear stress evolution parallel to the fault is quantified, first, using surface displacement measurements at a low frequency of 0.002 Hz (one measure each 600s). Average yield stress is about 520 Pa at site 1 and 450 Pa at site 2. This difference is due to normal stress variations along the fault strike: average normal stress is 550 Pa and 480 Pa at site 1 and 2, respectively. Note that these values give an apparent friction coefficient of about 1 which is consistent with experimental measurements performed using a direct shear box device.

Figure 18b shows a more-detailed analysis of instantaneous stress variations using a higher sampling rate of 0.17 Hz (one measure each 6 s). At this resolution, it is possible to observe surface stress evolution at the scale of individual seismic cycles. As expected, each cycle is characterized by a progressive elastic loading phase followed by an abrupt stress drop. Here average cycle duration is about 90 s.

Static stress drop ($\Delta\tau$) can be determined using the shear modulus (G), the mean slip (u) on the fault plane, and a scale length (E) linked by the following equation [e.g., *Scholz*, 2002; *Kanamori*, 1994]:

$$\Delta\tau = \frac{Gu}{E} \tag{11}$$

The scale length could be the fault length L, the fault width W, or the square root of fault area S, depending on the fault geometry [*Kanamori*, 1994]. Typical large microquakes are characterized by a surface rupture of

0.5 m × 0.05 m and a mean coseismic slip of $u = 1.5 \times 10^{-4}$ m (see for instance Figure 16). Using the same model and nature physical and mechanical parameters as for the calculation of the seismic moment (see section 4.1): (1) a shear modulus $G = 45$ kPa, a mean coseismic slip of $u = 1.5 \times 10^{-4}$ m, and a fault surface $S = 0.035$ m^2 for the model and (2) a shear modulus of $G = 20$ GPa, a coseismic mean slip of $u = 5$ m and a fault surface $S = 1.4 \times 10^9$ m^2 for a $M_w = 7.5$ earthquake. Model and nature stress drops ($\Delta\tau$ Model and $\Delta\tau$ Nature) can be evaluated to 42 Pa and 3 MPa, respectively. Based on these calculations, the average model to nature stress drop ratio is estimated to $\Delta\tau^* \sim 1.4 \times 10^{-5}$ which is several time greater than the stress and geometric scaling factors (~$4–5 \times 10^{-6}$) even if remains in the same order of magnitude. This scaling distortion will be discussed later (section 5.2).

In the presented experiment (Figure 18), major stress drops range between 40 and 80 Pa and are generally detected on both sites, indicating that they are generated by strong microquakes rupturing most of the fault. Low stress drops range from a few Pascal up to 30–40 Pa and are generally detectable at only one site. These stress drops are associated to low and moderate microquakes rupturing a small portion of the fault.

It is interesting to observe that, in some cases, stress drop observed at one site can be associated with a slight stress increase on the other site and that a moderate microquake occurring on one site triggered another one near the other site (Figure 18b). These observations are consistent with coseismic stress transfer from one portion of the fault to the other when the considered site is located in the positive Coulomb stress change lobes induced by a distant microquake (as shown in Figure 14). This mechanical process has been evoked to explain time clustering of large earthquakes such as those that occurred on near faults in Mongolia during the twentieth century [e.g., *Chéry et al*., 2001b].

Model's capability to reproduce such mechanical behavior is of great interest since such study is almost impossible to perform for natural cases because subsurface stress field can be only estimated very punctually using deep borehole stress measurements and stress-induced wellbore breakouts in oil and gas wells or regionally using focal mechanism inversions [*Zoback et al*., 1987; *Fuchs and Müller*, 2001; *Townend and Zoback*, 2004]. In the last case, only *P* and *T* axis directions can be estimated.

5. Discussion

Considering the objectives of this methodological paper, three main points of interest can be discussed; (1) model limitations, (2) model scaling evaluation, (3) model potentialities and forthcoming scientific investigations, including planned technical and thematic developments.

5.1. Model Limitations

The model is still, of course, oversimplified compared to nature. Its multilayered rheology only accounts for first-order mechanical properties of the continental crust [e.g., *Byerlee*, 1978; *Paterson and Luan*, 1990]. The effects of temperature and pressure which control, among others, metamorphism and phase change cannot be simulated experimentally. Density contrast between upper and lower crust is also unrealistic even if this feature is partly compensated by imposing the initial normal stress and by the pure strike-slip kinematics of model deformation.

Several geological processes are not considered such as fluid pressure that plays a likely significant role in fault weakening and aseismic creep triggering [e.g., *Bizzarri*, 2009; *Faulkner and Rutter*, 2001]. The simulated upper crust is only capable to deform elastically, plastic deformation processes in the upper crust, including folding and pressure/dissolution are not simulated.

Model fault plane is imposed, and its geometric characteristics remain fixed during the whole experiment duration. In nature, fault segmentation related to changes in fault strike, fault lengthening, and inherited lithological heterogeneities are observed [e.g., *Sylvester*, 1988].

5.2. Model Scaling Evaluation

As demonstrated by the experimental results presented in the previous section of this paper, model scaling appears to be satisfactory but, of course, cannot be considered as rigorous. Table 1 summarizes the main scaling parameters derived from the quantitative analysis of model dynamics and the comparison with natural earthquake kinematics and mechanics. At first order, the model seems properly

scaled in terms of geometry, kinematics and stress properties that are all controlled by a scaling ratio ranging from 3×10^{-6} to 5×10^{-6}. This ratio was anticipated to satisfy the technical constraints of the experimental device.

Against requirement of the scaling rules, some dimensionless parameters differ from their natural counterparts; the Poisson ratio is too low (0.06 instead of 0.25) and the static friction is still a little bit too high (0.7–1 instead of 0.2–0.4). Additionally, two other scaling parameters show some discrepancy with expected scaling factor; coseismic fault slip, and associated stress drop appears higher than the geometric factor by one order of magnitude ($1–3\times10^{-5}$ instead of 3 to 4×10^{-6}). This feature affects also the fault slip gradients that are in the same order but higher than expected (10^{-3} to 10^{-5} instead of 10^{-4} to 10^{-6}). These scaling distortions have a positive impact since they facilitate model monitoring in exaggerating model deformation. However, their origin should be determined. We propose that this discrepancy may be related either to (1) rheological properties of the polyurethane foam or to (2) kinematics and geometric imposed boundary conditions. The first explanation refers to results of previous experiments showing that using a more rigid foam (higher Young's modulus), coseismic slip gradients decrease because the rupture length increases more significantly than coseismic fault slip. The second explanation is related to the velocity-strengthening low-friction patches at the fault tips that act as barriers to the rupture propagation of slip events. Slip decreases thus much more rapidly from the maximum slip to the fault ends than in the absence of patches. Using of larger model dimensions could solve this problem, but affecting the accuracy and spatial resolution measurements of surface displacements.

Concerning the temporal scaling (1 s equal 10–15 years), model to nature comparison show that, at first order, it is acceptable. Coseismic and interseismic phase durations and mean velocities are a little bit overestimated but remain in the right order of magnitude. Using a silicone layer with a higher viscosity will probably improve these points.

5.3. Model Potentialities and Forthcoming Scientific Investigations

The experimental model shows striking analogies with nature in terms of kinematical and mechanical behaviors and high scientific potential:

1. Thanks to its visco-elasto-plastic multilayered rheology, the model is capable to reproduce the main deformation stages of the seismic cycle; the interseismic and the coseismic phases including associated seismic and aseismic behaviors.
2. The postseismic phase is also well reproduced, including after slip and viscoelastic relaxation behaviors whose kinematical and mechanical characteristics compare well with nature.
3. The use of numerical modeling tools, mainly derived from those used to study natural earthquakes, gives access to key parameters such as the strain and stress fields at the surface and at depth and also the slip and stress distributions along the fault plane.
4. The analog model generates a broad variability of earthquake like slip events constituting large data catalogs that can be used to study the scaling laws that control fault slip dynamics.
5. Similarly, the model generates hundreds of successive seismic cycles allowing access to both short-term and long-term evolution of strain and stress fields. This is of great interest to investigate, using statistical and probabilistic approaches, earthquake predictability in particular to determine future event magnitudes and locations.
6. Preliminary results demonstrate that the study of rupture dynamics will be an interesting goal to achieve. Presently, using the higher available measurement sampling rate (Full HD camera, 25 Hz, equivalent to several months in nature), a detailed analysis of the coseismic phase is not possible (Figure 13a). To access the kinematics of rupture propagation, we are implementing a high-speed video imagery (500–1000 Hz sampling rate) to record time series with up to 50 images of the rupture propagation.
7. In complement to the high-frequency surface kinematic measurements, we plan to deploy a network of accelerometers (type MEMS, micro-electro-mechanical sensor) in order to analyze the seismic signals generated by the microearthquakes. First tests (Figure 13b) show that these data should permit a seismological study of the analog model by using a kinematic inversion method based on the discrete wave number approach proposed by *Bouchon* [1981], modified by *Favreau et al*. [2010], coupled with an inversion method [*Sambridge*, 1999] scaled to the size of the analog earthquakes.

6. Conclusions

We have developed a new experimental setup dedicated to the study of seismic cycle crustal deformation associated to strike-slip faulting. Our analog model integrates simple but realistic tectonics and kinematics boundary conditions together with a multilayer visco-elasto-plastic rheology simulating the upper and lower crust deformation behavior. Another originality of our approach is the use of numerical modeling algorithms to investigate the distribution and evolution of strain and stress at the surface and at depth, along the fault plane.

First results, based on more than 50 experiments, show that our model succeed in reproducing the deformation mechanisms and surface kinematics associated to the main phases of the seismic cycle as defined by the elastic rebound theory [*Reid*, 1910].

Model interseismic deformation is characterized by either total or partial locking of the fault associated to episodic aseismic creep events. Model surface kinematics can be predicted using the *Savage and Burford* [1973] analytical formulation which validate the good analogy with nature. Coseismic deformation is characterized by almost instantaneous fault slip events that present a broad variability in size and location along the fault. Here also, surface kinematics associated to these microquakes is consistent to those predicted using half-space elastic dislocation numerical modeling.

Finally, the postseismic deformation exhibits after-slip on the fault plane and can be also associated to viscoelastic relaxation of the simulated lower crust due to the mechanical readjustment at the brittle-ductile transition.

Consequently, we consider that model scaling, despite inevitable dissimilarities, is satisfactory and allow extrapolation of first-order experimental results to nature taking into account intrinsic model limitations. Some scientific results have been already obtained and are in the process of submission. They concern interesting relations between fault mechanical behavior and the role of some key parameters such as the normal stress, the loading rate, and the frictional heterogeneity along the fault.

Future technical developments are on the way, mainly to improve model scaling and to access to coseismic rupture propagation analysis. Moreover, we plan to test specific devices to measure the vertical component of displacement (laser holography), accelerations, and stresses (microsensors) during experiments.

Acknowledgments

Data supporting Figures 12, 17, and 18 are available as in supporting informations Table S1, S2, and S3, respectively. This project has been funded by INSU and CNRS grants. We are very grateful to the two reviewers Fabio Corbi and Stefan Nielsen for thorough and constructive comments they made on the original version of our work. We thanks J. Chéry, J. Malavieille, and S. Peyrat for fruitful discussions.

References

Ambraseys, N. N., and C. F. Finkel (1995), The seismicity of Turkey and adjacent areas: A historical review, 1500–1800, M.S. Eren, Beyoğlu, İstanbul.

Anooshehpoor, A., and J. N. Brune (1994), Frictional heat generation and seismic radiation in a foam rubber model of earthquakes, *Pure Appl. Geophys.*, *142*(3–4), 735–747, doi:10.1007/BF00876062.

Anooshehpoor, A., and J. N. Brune (1999), Wrinkle-like Weertman pulse at the interface between two blocks of foam rubber with different velocities, *Geophys. Res. Lett.*, *26*(13), 2025–2028, doi:10.1029/1999GL900397.

Armijo, R., et al. (2005), Submarine fault scarps in the Sea of Marmara pull-apart (North Anatolian Fault): Implications for seismic hazard in Istanbul, *Geochem. Geophys. Geosyst.*, *6*, Q06009, doi:10.1029/2004GC000896.

Atzori, S., and A. Antonioli (2011), Optimal fault resolution in geodetic inversion of coseismic data, *Geophys. J. Int.*, *185*(1), 529–538, doi:10.1111/j.1365-246X.2011.04955.x.

Avouac, J.-P., F. Ayoub, S. Leprince, O. Konca, and D. V. Helmberger (2006), The 2005, M-w 7.6 Kashmir earthquake: Sub-pixel correlation of ASTER images and seismic waveforms analysis, *Earth Planet. Sci. Lett.*, *249*(3–4), 514–528, doi:10.1016/j.epsl.2006.06.025.

Avouac, J.-P., F. Ayoub, S. Wei, J.-P. Ampuero, L. Meng, S. Leprince, R. Jolivet, Z. Duputel, and D. Helmberger (2014), The 2013, Mw 7.7 Balochistan earthquake, energetic strike-slip reactivation of a thrust fault, *Earth Planet. Sci. Lett.*, *391*, 128–134, doi:10.1016/j.epsl.2014.01.036.

Baby, P., B. Colletta, and D. Zubieta (1995), Etude géométrique et expérimentale d'un bassin transporté: Exemple du synclinorium de l'Alto Beni (Andes centrales), *Bull. Soc. Geol. Fr.*, *166*(6), 797–811.

Barenblatt, G. I. (1962), The mathematical theory of equilibrium cracks in brittle fracture, *Adv. Appl. Mech.*, *7*, 55–129.

Barka, A. (1996), Slip distribution along the North Anatolian Fault associated with the large earthquakes of the period 1939 to 1967, *Bull. Seismol. Soc. Am.*, *86*(5), 1238–1254.

Barka, A. A. (1992), The North Anatolian fault zone, *Ann. Tecton.*, *6*, 164–195.

Ben-Zion, Y. (2008), Collective behavior of earthquakes and faults: Continuum-discrete transitions, progressive evolutionary changes, and different dynamic regimes, *Rev. Geophys.*, *46*, RG4006, doi:10.1029/2008RG000260.

Ben-Zion, Y., J. R. Rice, and R. Dmowska (1993), Interaction of the San Andreas Fault creeping segment with adjacent great rupture zones and earthquake recurrence at Parkfield, *J. Geophys. Res.*, *98*(B2), 2135–2144, doi:10.1029/92JB02154.

Bizzarri, A. (2009), What does control earthquake ruptures and dynamic faulting? A review of different competing mechanisms, in *Rock Physics and Natural Hazards*, edited by S. Vinciguerra and Y. Bernabé, pp. 741–776, Birkhäuser Basel, Berlin.

Blanpied, M. L., D. A. Lockner, and J. D. Byerlee (1991), Fault stability inferred from granite sliding experiments at hydrothermal conditions, *Geophys. Res. Lett.*, *18*(4), 609–612, doi:10.1029/91GL00469.

Bonini, M., D. Sokoutis, G. Mulugeta, and E. Katrivanos (2000), Modelling hanging wall accommodation above rigid thrust ramps, *J. Struct. Geol.*, *22*(8), 1165–1179, doi:10.1016/S0191-8141(00)00033-X.

Bouchon, M. (1981), A simple method to calculate Green's functions for elastic layered media, *Bull. Seismol. Soc. Am.*, *71*(4), 959–971.
Bouchon, M., M. Nafi Toksöz, H. Karabulut, M.-P. Bouin, M. Dietrich, M. Aktar, and M. Edie (2002), Space and time evolution of rupture and faulting during the 1999 İzmit (Turkey) earthquake, *Bull. Seismol. Soc. Am.*, *92*(1), 256–266.
Bouchon, M., H. Karabulut, M.-P. Bouin, J. Schmittbuhl, M. Vallée, R. Archuleta, S. Das, F. Renard, and D. Marsan (2010), Faulting characteristics of supershear earthquakes, *Tectonophysics*, *493*, 244–253.
Boutelier, D., C. Schrank, and A. Cruden (2008), Power-law viscous materials for analogue experiments: New data on the rheology of highly-filled silicone polymers, *J. Struct. Geol.*, *30*, 341–353, doi:10.1016/j.jsg.2007.10.009.
Brace, W. F. (1972), Laboratory studies of stick–slip and their application to earthquakes, *Tectonophysics*, *14*(3–4), 189–200, doi:10.1016/0040-1951(72)90068-6.
Brace, W. F., and J. D. Byerlee (1966), Stick–slip as a mechanism for earthquakes, *Science*, *153*(3739), 990–992, doi:10.1126/science.153.3739.990.
Bruhat, L., S. Barbot, and J.-P. Avouac (2011), Evidence for postseismic deformation of the lower crust following the 2004 Mw6.0 Parkfield earthquake, *J. Geophys. Res.*, *116*, B08401, doi:10.1029/2010JB008073.
Brune, J. N. (1973), Earthquake modeling by stick–slip along precut surfaces in stressed foam rubber, *Bull. Seismol. Soc. Am.*, *63*(6–1), 2105–2119.
Brune, J. N. (1996), Particle motions in a physical model of shallow angle thrust faulting, *Proc. Indian Acad. Sci. (Earth Planet. Sci.)*, *105*(2), 197–206, doi:10.1007/BF02876014.
Brune, J. N., and A. Anooshehpoor (1998), A physical model of the effect of a shallow weak layer on strong ground motion for strike-slip ruptures, *Bull. Seismol. Soc. Am.*, *88*(4), 1070–1078.
Bufe, C., and D. Varnes (1993), Predictive modeling of the seismic cycle of the Greater San-Francisco Bay-Region, *J. Geophys. Res.*, *98*(B6), 9871–9883, doi:10.1029/93JB00357.
Bürgmann, R., and G. Dresen (2008), Rheology of the lower crust and upper mantle: Evidence from rock mechanics, geodesy, and field observations, *Annu. Rev. Earth Planet. Sci.*, *36*, 531–567, doi:10.1146/annurev.earth.36.031207.124326.
Bürgmann, R., D. D. Pollard, and S. J. Martel (1994), Slip distributions on faults: Effects of stress gradients, inelastic deformation, heterogeneous host-rock stiffness, and fault interaction, *J. Struct. Geol.*, *16*(12), 1675–1690, doi:10.1016/0191-8141(94)90134-1.
Burridge, R., and L. Knopoff (1967), Model and theoretical seismicity, *Bull. Seismol. Soc. Am.*, *57*(3), 341–371.
Byerlee, J. D. (1968), Brittle-ductile transition in rocks, *J. Geophys. Res.*, *73*(14), 4741–4750, doi:10.1029/JB073i014p04741.
Byerlee, J. D. (1970), The mechanics of stick–slip, *Tectonophysics*, *9*(5), 475–486, doi:10.1016/0040-1951(70)90059-4.
Byerlee, J. D. (1978), Friction of rocks, *Pure Appl. Geophys.*, *116*(4–5), 615–626, doi:10.1007/BF00876528.
Cakir, Z., A. M. Akoglu, S. Belabbes, S. Ergintav, and M. Meghraoui (2005), Creeping along the Ismetpasa section of the North Anatolian Fault (Western Turkey): Rate and extent from InSAR, *Earth Planet. Sci. Lett.*, *238*(1–2), 225–234, doi:10.1016/j.epsl.2005.06.044.
Carlson, J. M., and J. S. Langer (1989), Mechanical model of an earthquake fault, *Phys. Rev. A*, *40*(11), 6470–6484, doi:10.1103/PhysRevA.40.6470.
Cartwright, J., and C. Mansfield (1998), Lateral displacement variation and lateral tip geometry of normal faults in the Canyonlands National Park, Utah, *J. Struct. Geol.*, *20*(1), 3–19.
Chéry, J. (2008), Geodetic strain across the San Andreas Fault reflects elastic plate thickness variations (rather than fault slip rate), *Earth Planet. Sci. Lett.*, *269*(3–4), 352–365, doi:10.1016/j.epsl.2008.01.046.
Chéry, J., M. D. Zoback, and R. Hassani (2001a), An integrated mechanical model of the San Andreas Fault in central and northern California, *J. Geophys. Res.*, *106*(B10), 22,051–22,066, doi:10.1029/2001JB000382.
Chéry, J., S. Carretier, and J.-F. Ritz (2001b), Postseismic stress transfer explains time clustering of large earthquakes in Mongolia, *Earth Planet. Sci. Lett.*, *194*(1–2), 277–286, doi:10.1016/S0012-821X(01)00552-0.
Chéry, J., M. D. Zoback, and R. Hassani (2001c), Rheology, strain and stress of the San Andreas Fault in Central and Northern California: A 3-D thermomechanical modeling study, *J. Geophys. Res.*, *106*, 22,051–22,066, doi:10.1029/2001JB000382.
Chinnery, M. A. (1961), The deformation of the ground around surface faults, *Bull. Seismol. Soc. Am.*, *51*(3), 355–372.
Chinnery, M. A. (1963), The stress changes that accompany strike-slip faulting, *Bull. Seismol. Soc. Am.*, *53*(5), 921–932.
Cobbold, P. R., and M. P. A. Jackson (1992), Gum rosin (colophony): A suitable material for thermomechanical modelling of the lithosphere, *Tectonophysics*, *210*(3–4), 255–271, doi:10.1016/0040-1951(92)90325-Z.
Coleman, T. F., and Y. Y. Li (1996), A reflective Newton method for minimizing a quadratic function subject to bounds on some of the variables, *SIAM J. Optim.*, *6*(4), 1040–1058, doi:10.1137/S1052623494240456.
Corbi, F., F. Funiciello, C. Faccenna, G. Ranalli, and A. Heuret (2011), Seismic variability of subduction thrust faults: Insights from laboratory models, *J. Geophys. Res.*, *116*, B06304, doi:10.1029/2010JB007993.
Corbi, F., F. Funiciello, M. Moroni, Y. van Dinther, P. M. Mai, L. A. Dalguer, and C. Faccenna (2013), The seismic cycle at subduction thrusts: 1. Insights from laboratory models, *J. Geophys. Res. Solid Earth*, *118*, 1483–1501, doi:10.1029/2012JB009481.
Davy, P., and P. Cobbold (1991), Experiments on shortening of a 4-layer model of the continental lithosphere, *Tectonophysics*, *188*(1–2), 1–25, doi:10.1016/0040-1951(91)90311-F.
Dawers, N. H., and M. H. Anders (1995), Displacement-length scaling and fault linkage, *J. Struct. Geol.*, *17*(5), 607–614, doi:10.1016/0191-8141(94)00091-D.
Delouis, B., D. Giardini, P. Lundgren, and J. Salichon (2002), Joint inversion of INSAR, GPS, teleseismic, and strong-motion data for the spatial and temporal distribution of earthquake slip: Application to the 1999 I'zmit mainshock, *Bull. Seismol. Soc. Am.*, *92*, 278–299.
Di Giuseppe, E., F. Funiciello, F. Corbi, G. Ranalli, and G. Mojoli (2009), Gelatins as rock analogs: A systematic study of their rheological and physical properties, *Tectonophysics*, *473*, 391–403, doi:10.1016/j.tecto.2009.03.012.
Dieterich, J. H. (1972), Time-dependent friction as a possible mechanism for aftershocks, *J. Geophys. Res.*, *77*(20), 3771–3781, doi:10.1029/JB077i020p03771.
Dieterich, J. H. (1992), Earthquake nucleation on faults with rate-and state-dependent strength, *Tectonophysics*, *211*(1–4), 115–134, doi:10.1016/0040-1951(92)90055-B.
Dominguez, S., J.-P. Avouac, and R. Michel (2003), Horizontal coseismic deformation of the 1999 Chi-Chi earthquake measured from SPOT satellite images: Implications for the seismic cycle along the western foothills of central Taiwan, *J. Geophys. Res.*, *108*(B2), 2083, doi:10.1029/2001JB000951.
Dugdale, D. S. (1960), Yielding of steel sheets containing slits, *J. Mech. Phys. Solids*, *8*(2), 100–104, doi:10.1016/0022-5096(60)90013-2.
Faccenna, C., D. Giardini, P. Davy, and A. Argentieri (1999), Initiation of subduction at Atlantic-type margins: Insights from laboratory experiments, *J. Geophys. Res.*, *104*(B2), 2749–2766, doi:10.1029/1998JB900072.
Faulkner, D. R., and E. H. Rutter (2001), Can the maintenance of overpressured fluids in large strike-slip fault zones explain their apparent weakness?, *Geology*, *29*(6), 503–506, doi:10.1130/0091-7613(2001)029<0503:CTMOOF>2.0.CO;2.
Favreau, P., A. Mangeney, A. Lucas, G. Crosta, and F. Bouchut (2010), Numerical modeling of landquakes, *Geophys. Res. Lett.*, *37*, L15305, doi:10.1029/2010GL043512.

Fialko, Y. (2004a), Evidence of fluid-filled upper crust from observations of postseismic deformation due to the 1992 Mw7.3 Landers earthquake, *J. Geophys. Res.*, *109*, B08401, doi:10.1029/2004JB002985.
Fialko, Y. (2004b), Probing the mechanical properties of seismically active crust with space geodesy: Study of the coseismic deformation due to the 1992 Mw7.3 Landers (southern California) earthquake, *J. Geophys. Res.*, *109*, B03307, doi:10.1029/2003JB002756.
Fuchs, K., and B. Müller (2001), World stress map of the Earth: A key to tectonic processes and technological applications, *Naturwissenschaften*, *88*(9), 357–371.
Goldfinger, C., Y. Ikeda, R. S. Yeats, and J. Ren (2013), Superquakes and supercycles, *Seismol. Res. Lett.*, *84*, 24–32, doi:10.1785/0220110135.
Grant, L. B., and K. Sieh (1994), Paleoseismic evidence of clustered earthquakes on the San Andreas Fault in the Carrizo Plain, California, *J. Geophys. Res.*, *99*(B4), 6819–6841, doi:10.1029/94JB00125.
Hamilton, T., and J. Mccloskey (1997), Breakdown in power-law scaling in an analogue model of earthquake rupture and stick–slip, *Geophys. Res. Lett.*, *24*(4), 465–468, doi:10.1029/97GL00203.
Horsfield, W. T. (1977), An experimental approach to basement-controlled faulting, *Geol. Mijnbouw*, *56*, 363–370.
Hubbert, M. K. (1937), Theory of scale models as applied to the study of geologic structures, *Bull. Geol. Soc. Am.*, *48*, 1459–1520.
Ikeda, Y., Y. Suzuki, E. Herece, F. Şaroğlu, A. M. Isikara, and Y. Honkura (1991), Geological evidence for the last two faulting events on the north Anatolian Fault zone in the Mudurnu Valley, western Turkey, *Tectonophysics*, *193*(4), 335–345, doi:10.1016/0040-1951(91)90342-P.
Jaeger, J. C., and N. G. W. Cook (1979), *Fundamentals of Rock Mechanics*, Chapman and Hall, Oxford, U. K.
Jolivet, R., R. Cattin, N. Chamotrooke, C. Lasserre, and G. Peltzer (2008), Thin-plate modeling of interseismic deformation and asymmetry across the Altyn Tagh fault zone, *Geophys. Res. Lett.*, *35*, L02309, doi:10.1029/2007GL031511.
Jolivet, R., et al. (2014), The 2013 Mw 7.7 Balochistan Earthquake: Seismic potential of an accretionary wedge, *Bull. Seismol. Soc. Am.*, *104*(2), 1020–1030, doi:10.1785/0120130313.
Kanamori, H. (1994), Mechanics of earthquakes, *Annu. Rev. Earth Planet. Sci.*, *22*(1), 207–237, doi:10.1146/annurev.ea.22.050194.001231.
Kanninen, M. F., and C. H. Popelar (1985), *Advanced Fracture Mechanics*, Oxford Univ. Press, New York.
Kim, Y.-S., and D. J. Sanderson (2005), The relationship between displacement and length of faults: A review, *Earth Sci. Rev.*, *68*(3–4), 317–334, doi:10.1016/j.earscirev.2004.06.003.
King, G., R. Stein, and J. Lin (1994), Static stress changes and the triggering of earthquakes, *Bull. Seismol. Soc. Am.*, *84*(3), 935–953.
Koyi, H. A., and A. Skelton (2001), Centrifuge modelling of the evolution of low-angle detachment faults from high-angle normal faults, *J. Struct. Geol.*, *23*(8), 1179–1185, doi:10.1016/S0191-8141(00)00185-1.
Lapusta, N., J. R. Rice, Y. Ben-Zion, and G. T. Zheng (2000), Elastodynamic analysis for slow tectonic loading with spontaneous rupture episodes on faults with rate- and state-dependent friction, *J. Geophys. Res.*, *105*(B10), 23,765–23,789, doi:10.1029/2000JB900250.
Latour, S., M. Campillo, C. Voisin, I. R. Ionescu, J. Schmedes, and D. Lavallee (2011a), Effective friction law for small-scale fault heterogeneity in 3D dynamic rupture, *J. Geophys. Res.*, *116*, B10306, doi:10.1029/2010JB008118.
Latour, S., T. Gallot, S. Catheline, C. Voisin, F. Renard, E. Larose, and M. Campillo (2011b), Ultrafast ultrasonic imaging of dynamic sliding friction in soft solids: The slow slip and the super-shear regimes, *Europhys. Lett.*, *96*(5), 59,003, doi:10.1209/0295-5075/96/59003.
Latour, S., C. Voisin, F. Renard, E. Larose, S. Catheline, and M. Campillo (2013), Effect of fault heterogeneity on rupture dynamics: An experimental approach using ultrafast ultrasonic imaging, *J. Geophys. Res. Solid Earth*, *118*, 5888–5902, doi:10.1002/2013JB010231.
Le Pichon, X., et al. (2001), The active Main Marmara Fault, *Earth Planet. Sci. Lett.*, *192*(4), 595–616, doi:10.1016/S0012-821X(01)00449-6.
Leprince, S., S. Barbot, F. Ayoub, and J.-P. Avouac (2007), Automatic and precise orthorectification, coregistration, and subpixel correlation of satellite images, application to ground deformation measurements, *IEEE Trans. Geosci. Remote Sens.*, *45*(6), 1529–1558, doi:10.1109/TGRS.2006.888937.
Li, V., and J. Rice (1987), Crustal deformation in Great California earthquake cycles, *J. Geophys. Res.*, *92*(B11), 11,533–11,551, doi:10.1029/JB092iB11p11533.
Lisowski, M. (1991), Recent plate motions and crustal deformation, *Rev. Geophys.*, *29*, 162–171.
Lykotrafitis, G., A. J. Rosakis, and G. Ravichandran (2006), Self-healing pulse-like shear ruptures in the laboratory, *Science*, *313*(5794), 1765–1768, doi:10.1126/science.1128359.
Manighetti, I., M. Campillo, C. Sammis, P. M. Mai, and G. King (2005), Evidence for self-similar, triangular slip distributions on earthquakes: Implications for earthquake and fault mechanics, *J. Geophys. Res.*, *110*, B05302, doi:10.1029/2004JB003174.
Manighetti, I., M. Campillo, S. Bouley, and F. Cotton (2007), Earthquake scaling, fault segmentation, and structural maturity, *Earth Planet. Sci. Lett.*, *253*, 429–438, doi:10.1016/j.epsl.2006.11.004.
Marone, C. (1998), Laboratory-derived friction laws and their application to seismic faulting, *Annu. Rev. Earth Planet. Sci.*, *26*(1), 643–696, doi:10.1146/annurev.earth.26.1.643.
Marone, C., C. B. Raleigh, and C. H. Scholz (1990), Frictional behavior and constitutive modeling of simulated fault gouge, *J. Geophys. Res.*, *95*(B5), 7007–7025, doi:10.1029/JB095iB05p07007.
Marone, C. J., C. H. Scholtz, and R. Bilham (1991), On the mechanics of earthquake afterslip, *J. Geophys. Res.*, *96*(B5), 8441–8452, doi:10.1029/91JB00275.
Martel, S. J., and C. Shacat (2006), Mechanics and interpretations of fault slip, in *Earthquakes: Radiated Energy and the Physics of Faulting*, edited by R. Abercrombie et al., pp. 207–215, AGU, Washington, D. C.
Matsuura, M., and T. Sato (1989), A dislocation model for the earthquake cycle at convergent plate boundaries, *Geophys. J. Int.*, *96*(1), 23–32, doi:10.1111/j.1365-246X.1989.tb05247.x.
Meade, B. J. (2007), Present-day kinematics at the India-Asia collision zone, *Geology*, *35*(1), 81–84, doi:10.1130/G22924A.1.
Meade, B. J., and B. H. Hager (2005), Block models of crustal motion in southern California constrained by GPS measurements, *J. Geophys. Res.*, *110*, B03403, doi:10.1029/2004JB003209.
Mello, M., H. S. Bhat, A. J. Rosakis, and H. Kanamori (2010), Identifying the unique ground motion signatures of supershear earthquakes: Theory and experiments, *Tectonophysics*, *493*(3–4), 297–326, doi:10.1016/j.tecto.2010.07.003.
Michel, R., and J. P. Avouac (2002), Deformation due to the 17 August 1999 Izmit, Turkey, earthquake measured from SPOT images, *J. Geophys. Res.*, *107*(B4), 2062, doi:10.1029/2000JB000102.
Montési, L. G. J. (2004), Controls of shear zone rheology and tectonic loading on postseismic creep, *J. Geophys. Res.*, *109*, B10404, doi:10.1029/2003JB002925.
Nalbant, S. S., and J. McCloskey (2011), Stress evolution before and after the 2008 Wenchuan, China earthquake, *Earth Planet. Sci. Lett.*, *307*(1–2), 222–232, doi:10.1016/j.epsl.2011.04.039.
Nalbant, S. S., A. Hubert, and G. C. P. King (1998), Stress coupling between earthquakes in northwest Turkey and the north Aegean Sea, *J. Geophys. Res.*, *103*(B10), 24,469–24,486, doi:10.1029/98JB01491.
Nasuno, S., A. Kudrolli, A. Bak, and J. P. Gollub (1998), Time-resolved studies of stick–slip friction in sheared granular layers, *Phys. Rev. E*, *58*(2), 2161–2171, doi:10.1103/PhysRevE.58.2161.

Nielsen, S., J. Taddeucci, and S. Vinciguerra (2010), Experimental observation of stick–slip instability fronts, *Geophys. J. Int.*, *180*(2), 697–702, doi:10.1111/j.1365-246X.2009.04444.x.
Nur, A., and G. Mavko (1974), Postseismic viscoelastic rebound, *Science*, *183*(4121), 204–206, doi:10.1126/science.183.4121.204.
Ohnaka, M. (1973), Experimental studies of stick–slip and their application to the earthquake source mechanism, *J. Phys. Earth*, *21*(3), 285–303, doi:10.4294/jpe1952.21.285.
Ohnaka, M., Y. Kuwahara, and K. Yamamoto (1987), Constitutive relations between dynamic physical parameters near a tip of the propagating slip zone during stick–slip shear failure, *Tectonophysics*, *144*(1–3), 109–125, doi:10.1016/0040-1951(87)90011-4.
Okada, Y. (1985), Surface deformation due to shear and tensile faults in a half-space, *Bull. Seismol. Soc. Am.*, *75*(4), 1135–1154.
Okada, Y. (1992), Internal deformation due to shear and tensile faults in a half-space, *Bull. Seismol. Soc. Am.*, *82*(2), 1018–1040.
Page, M. T., S. Custodio, R. J. Archuleta, and J. M. Carlson (2009), Constraining earthquake source inversions with GPS data: 1. Resolution-based removal of artifacts, *J. Geophys. Res.*, *114*, B01314, doi:10.1029/2007JB005449.
Passelegue, F. X., A. Schubnel, S. Nielsen, H. S. Bhat, and R. Madariaga (2013), From sub-Rayleigh to supershear ruptures during stick–slip experiments on crustal rocks, *Science*, *340*(6137), 1208–1211, doi:10.1126/science.1235637.
Paterson, M. S., and F. C. Luan (1990), Quartzite rheology under geological conditions, in *Deformation Mechanisms, Rheology and Tectonics*, edited by R. J. Knipe and E. H. Rutter, *Geol. Soc. London Spec. Pub.*, *54*, 299–307.
Peltzer, G. (1999), Evidence of nonlinear elasticity of the crust from the Mw7.6 Manyi (Tibet) Earthquake, *Science*, *286*(5438), 272–276.
Perfettini, H., and J. P. Avouac (2004), Stress transfer and strain rate variations during the seismic cycle, *J. Geophys. Res.*, *109*, B06402, doi:10.1029/2003JB002917.
Perfettini, H., and J.-P. Avouac (2007), Modeling afterslip and aftershocks following the 1992 Landers earthquake, *J. Geophys. Res.*, *112*, B07409, doi:10.1029/2006JB004399.
Petit, J.-P., and M. Barquins (1988), Can natural faults propagate under Mode II conditions?, *Tectonics*, *7*(6), 1243–1256, doi:10.1029/TC007i006p01243.
Pollard, D. D., and P. Segall (1987), Theoretical displacements and stresses near fractures in rock: With applications to faults, joints, veins, dikes, and solution surfaces, in *Fracture Mechanics of Rock*, edited by B. K. Atkinson, pp. 277–349, Academic Press, London.
Pollitz, F. F., C. Wicks, and W. Thatcher (2001), Mantle flow beneath a continental strike-slip fault: Postseismic deformation after the 1999 Hector Mine Earthquake, *Science*, *293*(5536), 1814–1818, doi:10.1126/science.1061361.
Pondard, N., R. Armijo, G. C. P. King, B. Meyer, and F. Flerit (2007), Fault interactions in the Sea of Marmara pull-apart (North Anatolian Fault): Earthquake clustering and propagating earthquake sequences, *Geophys. J. Int.*, *171*(3), 1185–1197, doi:10.1111/j.1365-246X.2007.03580.x.
Qu, C., G. Zhang, X. Shan, G. Zhang, X. Song, and Y. Liu (2013), Coseismic deformation derived from analyses of C and L band SAR data and fault slip inversion of the Yushu Ms7.1 earthquake, China in 2010, *Tectonophysics*, *584*, 119–128, doi:10.1016/j.tecto.2012.05.011.
Ramberg, H. (1981), *Gravity, Deformation, and the Earth's Crust*, 2nd ed., Academic Press Inc, London, New York.
Reid, H. F. (1910), The mechanics of the earthquake, the California Earthquake of April 18, 1906, in *Report of the State Earthquake Investigation Commission*, vol. 2, 192 pp., Carnegie Institution of Washington, Washington, D. C.
Reilinger, R. E., et al. (2000), Coseismic and postseismic fault slip for the 17 August 1999, M=7.5, Izmit, Turkey earthquake, *Science*, *289*(5484), 1519–1524, doi:10.1126/science.289.5484.1519.
Rosakis, A. J., O. Samudrala, and D. Coker (1999), Cracks faster than the shear wave speed, *Science*, *284*(5418), 1337–1340.
Rosenau, M., J. Lohrmann, and O. Oncken (2009), Shocks in a box: An analogue model of subduction earthquake cycles with application to seismotectonic forearc evolution, *J. Geophys. Res.*, *114*, B01409, doi:10.1029/2008JB005665.
Ruina, A. (1983), Slip instability and state variable friction laws, *J. Geophys. Res.*, *88*(B12), 10,359–10,370, doi:10.1029/JB088iB12p10359.
Sambridge, M. (1999), Geophysical inversion with a neighbourhood algorithm—I. Searching a parameter space, *Geophys. J. Int.*, *138*(2), 479–494, doi:10.1046/j.1365-246X.1999.00876.x.
Savage, J. (1983), A dislocation model of strain accumulation and release at a subduction zone, *J. Geophys. Res.*, *88*(NB6), 4984–4996, doi:10.1029/JB088iB06p04984.
Savage, J. C. (1980), *Dislocations in Seismology*, Elsevier, New York.
Savage, J. C. (1990), Equivalent strike-slip earthquake cycles in half-space and lithosphere-asthenosphere earth models, *J. Geophys. Res.*, *95*(B4), 4873–4879, doi:10.1029/JB095iB04p04873.
Savage, J. C., and R. O. Burford (1973), Geodetic determination of relative plate motion in central California, *J. Geophys. Res.*, *78*(5), 832–845, doi:10.1029/JB078i005p00832.
Savage, J. C., and L. M. Hastie (1966), Surface deformation associated with dip-slip faulting, *J. Geophys. Res.*, *71*(20), 4897–4904, doi:10.1029/JZ071i020p04897.
Savage, J. C., and W. H. Prescott (1978), Asthenosphere readjustment and the earthquake cycle, *J. Geophys. Res.*, *83*(B7), 3369–3376, doi:10.1029/JB083iB07p03369.
Schlagenhauf, A., I. Manighetti, L. Benedetti, Y. Gaudemer, R. Finkel, J. Malavieille, and K. Pou (2011), Earthquake supercycles in Central Italy, inferred from 36Cl exposure dating, *Earth Planet. Sci. Lett.*, *307*(3–4), 487–500, doi:10.1016/j.epsl.2011.05.022.
Schmalzle, G., T. Dixon, R. Malservisi, and R. Govers (2006), Strain accumulation across the Carrizo segment of the San Andreas Fault, California: Impact of laterally varying crustal properties, *J. Geophys. Res.*, *111*, B05403, doi:10.1029/2005JB003843.
Scholz, C. H. (1998), Earthquakes and friction laws, *Nature*, *391*(6662), 37–42, doi:10.1038/34097.
Scholz, C. H. (2002), *The Mechanics of Earthquakes and Faulting*, 2nd ed., Cambridge Univ. Press, Cambridge, U. K.
Schubnel, A., S. Nielsen, J. Taddeucci, S. Vinciguerra, and S. Rao (2011), Photo-acoustic study of subshear and supershear ruptures in the laboratory, *Earth Planet. Sci. Lett.*, *308*(3–4), 424–432, doi:10.1016/j.epsl.2011.06.013.
Schwartz, D. P., and K. J. Coppersmith (1984), Fault behavior and characteristic earthquakes: Examples from the Wasatch and San Andreas Fault Zones, *J. Geophys. Res.*, *89*(B7), 5681–5698, doi:10.1029/JB089iB07p05681.
Segall, P., and D. D. Pollard (1980), Mechanics of discontinuous faults, *J. Geophys. Res.*, *85*(B8), 4337–4350, doi:10.1029/JB085iB08p04337.
Sieh, K., D. H. Natawidjaja, A. J. Meltzner, C.-C. Shen, H. Cheng, K.-S. Li, B. W. Suwargadi, J. Galetzka, B. Philibosian, and R. L. Edwards (2008), Earthquake supercycles inferred from sea-level changes recorded in the corals of West Sumatra, *Science*, *322*(5908), 1674–1678, doi:10.1126/science.1163589.
Smith, S. W., and M. Wyss (1968), Displacement of the San Andreas Fault initiated by the 1966 Parkfield earthquake, *Bull. Seismol. Soc. Am.*, *68*, 1955–1974.
Soliva, R., and A. Benedicto (2005), Geometry, scaling relations and spacing of vertically restricted normal faults, *J. Struct. Geol.*, *27*(2), 317–325, doi:10.1016/j.jsg.2004.08.010.
Stein, R. S., A. A. Barka, and J. H. Dieterich (1997), Progressive failure on the North Anatolian Fault since 1939 by earthquake stress triggering, *Geophys. J. Int.*, *128*(3), 594–604, doi:10.1111/j.1365-246X.1997.tb05321.x.

Steketee, J. A. (1958a), On Volterra's dislocations in a semi-infinite elastic medium, *Can. J. Phys.*, *36*(2), 192–205, doi:10.1139/p58-024.
Steketee, J. A. (1958b), Some geophysical applications of the elasticity theory of dislocations, *Can. J. Phys.*, *36*(9), 1168–1198, doi:10.1139/p58-123.
Stesky, R. M., W. F. Brace, D. K. Riley, and P.-Y. F. Robin (1974), Friction in faulted rock at high temperature and pressure, *Tectonophysics*, *23*(1–2), 177–203, doi:10.1016/0040-1951(74)90119-X.
Sylvester, G. (1988), Strike-slip faults, *Geol. Soc. Am. Bull.*, *100*, 1666–1703.
Ten Grotenhuis, S. M., S. Piazolo, T. Pakula, C. W. Passchier, and P. D. Bons (2002), Are polymers suitable rock analogs?, *Tectonophysics*, *350*(1), 35–47, doi:10.1016/S0040-1951(02)00080-X.
Thatcher, W. (1983), Nonlinear strain buildup and the earthquake cycle on the San Andreas Fault, *J. Geophys. Res.*, *88*(B7), 5893–5902, doi:10.1029/JB088iB07p05893.
Thatcher, W., and J. Rundle (1984), A viscoelastic coupling model for the cyclic deformation due to periodically repeated earthquakes at subduction zones, *J. Geophys. Res.*, *89*(NB9), 7631–7640, doi:10.1029/JB089iB09p07631.
Titus, S. J., M. Dyson, C. DeMets, B. Tikoff, F. Rolandone, and R. Bürgmann (2011), Geologic versus geodetic deformation adjacent to the San Andreas Fault, central California, *Geol. Soc. Am. Bull.*, *123*(5–6), 794–820, doi:10.1130/B30150.1.
Townend, J., and M. D. Zoback (2004), Regional tectonic stress near the San Andreas Fault in central and southern California, *Geophys. Res. Lett.*, *31*, L15S11, doi:10.1029/2003GL018918.
Tse, S. T., and J. R. Rice (1986), Crustal earthquake instability in relation to the depth variation of frictional slip properties, *J. Geophys. Res.*, *91*(B9), 9452–9472, doi:10.1029/JB091iB09p09452.
Van Dinther, Y., T. V. Gerya, L. A. Dalguer, P. M. Mai, G. Morra, and D. Giardini (2013), The seismic cycle at subduction thrusts: Insights from seismo-thermo-mechanical models, *J. Geophys. Res. Solid Earth*, *118*, 6183–6202, doi:10.1002/2013JB010380.
Van Puymbroeck, N., R. Michel, R. Binet, J. P. Avouac, and J. Taboury (2000), Measuring earthquakes from optical satellite images, *Appl. Opt.*, *39*(20), 3486–3494, doi:10.1364/AO.39.003486.
Vergne, J., R. Cattin, and J. P. Avouac (2001), On the use of dislocations to model interseismic strain and stress build-up at intracontinental thrust faults, *Geophys. J. Int.*, *147*(1), 155–162, doi:10.1046/j.1365-246X.2001.00524.x.
Wald, D. J., T. H. Heaton, and K. W. Hudnut (1996), The slip history of the 1994 Northridge, California, earthquake determined from strong-motion, teleseismic, GPS, and leveling data, *Bull. Seismol. Soc. Am.*, *86*(1B), S49–S70.
Wang, J.-H. (2012), Some intrinsic properties of the two-dimensional dynamical spring-slider model of earthquake faults, *Bull. Seismol. Soc. Am.*, *102*(2), 822–835, doi:10.1785/0120110172.
Wang, K., T. Mulder, G. C. Rogers, and R. D. Hyndman (1995), Case for very low coupling stress on the Cascadia Ssubduction Fault, *J. Geophys. Res.*, *100*(B7), 12,907–12,918, doi:10.1029/95JB00516.
Wang, H., C. Xu, and L. Ge (2007), Coseismic deformation and slip distribution of the 1997 7.5 Manyi, Tibet, earthquake from InSAR measurements, *J. Geodyn.*, *44*(3–5), 200–212, doi:10.1016/j.jog.2007.03.003.
Wang, K., Y. Hu, and J. He (2012), Deformation cycles of subduction earthquakes in a viscoelastic Earth, *Nature*, *484*(7394), 327–332, doi:10.1038/nature11032.
Weertman, J., and J. R. Weertman (1964), *Elementary Dislocation Theory*, Macmillan, New York.
Weijermars, R. (1986), Flow behaviour and physical chemistry of bouncing putties and related polymers in view of tectonic laboratory applications, *Tectonophysics*, *124*(3–4), 325–358, doi:10.1016/0040-1951(86)90208-8.
Weijermars, R., and H. Schmeling (1986), Scaling of Newtonian and non-Newtonian fluid dynamics without inertia for quantitative modelling of rock flow due to gravity (including the concept of rheological similarity), *Phys. Earth Planet. Inter.*, *43*(4), 316–330, doi:10.1016/0031-9201(86)90021-X.
Weldon, R., K. Scharer, T. Fumal, and G. Biasi (2004), Wrightwood and the earthquake cycle: What a long recurrence record tells us about how faults work, *Geol. Soc. Am.*, *14*(9), 4–10, doi:10.1130/1052-5173(2004)014<4:WATECW>2.0.CO;2.
Wells, D., and K. Coppersmith (1994), New empirical relationships among magnitude, rupture length, rupture width, rupture area, and surface displacement, *Bull. Seismol. Soc. Am.*, *84*(4), 974–1002.
Wen, Y., Z. Li, C. Xu, I. Ryder, and R. Buergmann (2012), Postseismic motion after the 2001 M-W 7.8 Kokoxili earthquake in Tibet observed by InSAR time series, *J. Geophys. Res.*, *117*, B08405, doi:10.1029/2011JB009043.
Wesnousky, S. G. (2008), Displacement and geometrical characteristics of earthquake surface ruptures: Issues and implications for seismic-hazard analysis and the process of earthquake rupture, *Bull. Seismol. Soc. Am.*, *98*(4), 1609–1632, doi:10.1785/0120070111.
Willemse, E. J. M. (1997), Segmented normal faults: Correspondence between three-dimensional mechanical models and field data, *J. Geophys. Res.*, *102*, 675–692.
Xia, K. W., A. J. Rosakis, and H. Kanamori (2004), Laboratory earthquakes: The sub-Rayleigh-to-supershear rupture transition, *Science*, *303*(5665), 1859–1861.
Zoback, M. D., et al. (1987), New evidence on the state of stress of the San-Andreas fault system, *Science*, *238*(4830), 1105–1111.